CHALMERS
UNIVERSITY OF TECHNOLOGY

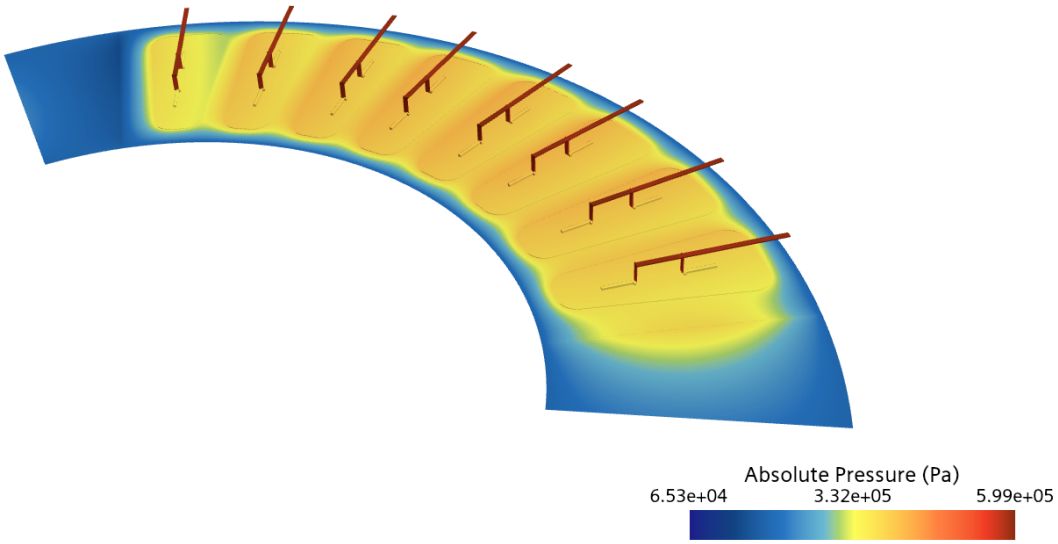

Evaluation and Analysis of Different Hydrostatic Bearing Designs Inside an Electrical Machine

Master's Thesis in Applied Mechanics

Oskar Ståhlbom

Department of Mechanics and Maritime Science

CHALMERS UNIVERSITY OF TECHNOLOGY
Gothenburg, Sweden 2025
www.chalmers.se

Master's thesis 2025

Evaluation and Analysis of Different Hydrostatic Bearing Designs Inside an Electrical Machine

Oskar Ståhlbom

CHALMERS
UNIVERSITY OF TECHNOLOGY

Department of Mechanics and Maritime Science
Division of Fluid Mechanics
Chalmers University of Technology
Gothenburg, Sweden 2025

Evaluation and Analysis of Different Hydrostatic Bearing Designs Inside an Electrical Machine
Oskar Ståhlbom

Supervisor: Anders Hagnestål, Hagnesia AB

Examiner: Huadong Yao, Department of Mechanics and Maritime Science, Chalmers University of Technology

Master's Thesis 2025
Department of Mechanics and Maritime Science
Division of Fluid Mechanics
Chalmers University of Technology
SE-412 96 Gothenburg
Telephone +46 31 772 1000

Cover: Absolute Pressure Over the Fluid Domain for the Basic Geometry

Typeset in LaTeX
Printed by Chalmers Reproservice
Gothenburg, Sweden 2025

Evaluation and Analysis of Different Hydrostatic Bearing Designs Inside an Electrical Machine
Oskar Ståhlbom
Department of Mechanics and Maritime Science
Chalmers University of Technology

Abstract

This report is a part of a master's thesis on evaluation and analysis of different hydrostatic fluid bearing designs which are employed inside an electrical machine. The evaluation is made numerically using Simcenter STAR-CCM+ (STAR-CCM+). A CAD model of the currently used fluid bearing design is provided which is then modified into different geometries, focusing on the recess pocket's shape and the fluid film thickness. The CAD models are imported into STAR-CCM+ and meshed taking the fundamentals of fluid mechanics, turbulence modelling and computational fluid dynamics into account. An unstructured trimmed cell mesher together with a prism layer mesher are used to mesh the domain. The fluid simulation was solved as a steady state incompressible liquid with mostly standardized settings. For the turbulence closure model the k-ω is used to provide a better solution in the viscous sublayer for better accuracy regarding the wall shear stress on the rotor. Appropriate boundary conditions are set up for the moving and stationary walls as well as for the inlets, outlets, symmetry planes, and interfaces for the periodicity.

Fluid simulations have been performed for a number of different geometries. A comparison between the different geometries' performance regarding maximum and minimum pressure, power consumption, risk of cavitation, and pressure distribution is made where it can be seen that the differences between the geometries are small. A comparison is also made for when the fluid film thickness over the lands increases or decreases linearly with an increasing radial coordinate. It can be seen that the difference between the simulated geometries in this case is more substantial, where a noticeable difference in the pressure distribution between the geometries can be seen but both configurations show a risk for cavitation. The conclusion from the calculations is that the pocket shape does not affect the power consumption in a significant way, although the size of the pockets influences the viscous friction losses and more shallow pockets display higher maximum pressures. Also, the calculations show that there is a risk of cavitation if the fluid bearing is unbalanced due to unbalanced magnetic forces.

Keywords: Computational Fluid Dynamics, Hydrostatic Bearing, Fluid Bearing, Axial Flux Machine, Electric Machine.

Acknowledgements

I first and foremost would like to express my sincere gratitude to Hagnesia for giving me the opportunity to carry out this thesis project. A special word of appreciation goes to Anders Hagnestål for taking his time to give guidance and technical knowledge which have been incredibly helpful and valuable. I am also very grateful to the team members at Hagnesia for welcoming me, always being willing to assist when needed, and for offering their expertise.

I would also like to give a thank you to my examiner Huadong Yao for his time, and very valuable guidance throughout this thesis. The development and completion of this work has been helped by his constructive feedback and support for which I am thankful for.

I am also very thankful for my family and friends who have supported me not only during this project, but throughout my entire education.

Oskar Ståhlbom, Gothenburg, June 2025

List of Acronyms

Below is the list of acronyms that have been used throughout this thesis listed in alphabetical order:

AFPM	Axial Flux Permanent Magnet
AF2SPM	Axial Flux Two Stator Permanent Magnet
AFTPM	Axial Flux Toroidal Permanent Magnet
CFD	Computational Fluid Dynamics
EM	Electrical Machine
IM	Induction Machine
NN	North to North
NS	North to South
RFPM	Radial Flux Permanent Magnet
STAR-CCM+	Simcenter STAR-CCM+

Nomenclature

Below is the nomenclature of indices and variables that have been used throughout this thesis.

Indices

i,j,k	Einstein Notation
t	Turbulent Viscosity

Variables

d	Characteristic Length
ρ	Density
ϵ	Dissipation Rate
$\mathbf{r}$	Distance Vector
μ	Dynamic Viscosity
$\mathbf{F}$	Force Vector
p	Hydrodynamic Pressure
ν	Kinematic Viscosity
δ_{ij}	Kroenecker Delta
P	Pressure
$\boldsymbol{\tau}$	Shear Stress Vector
S_M	Source Term
ω	Specific Dissipation Rate
t	Time
k	Turbulent Kinetic Energy
$\mathbf{M}$	Torque Vector
$\mathbf{u}$	Velocity Vector

u	Velocity in the X-Direction
v	Velocity in the Y-Direction
w	Velocity in the Z-Direction

Contents

List of Figures

List of Tables

1
Introduction

1.1 Background

Electrical machines (EM) includes both electrical motors and generators. They are used in a lot of different fields in today's society, from electric vehicles, electricity generation, household equipment, machinery, etc. Hagnesia AB is a Swedish company which is developing a new type of an axial flux electrical machine which has an advantage to the standard electrical machines used today for low speed applications, where it can reduce the material usage by up to 90 percent and increase the efficiency at low Revolutions Per Minute (RPM). A challenge with these machines is that they comprise thin rotating discs which are subjected to strong magnetic forces and need to be stabilized. In this work it is examined how a hydrostatic bearing solution to this challenge would perform.

1.1.1 Axial Flux Machines

The difference between radial and axial flux electrical machines is the direction of the magnetic flux. Radial flux machines have magnetic flux predominantly in the radial direction, and the airgap that separates the rotor from the stator forms a thin hollow cylinder. Axial flux machines, on the other hand, have magnetic flux predominantly in the axial direction, and the machines are often flat [1]. There are multiple types of electrical machines, such as induction machines, synchronous machines with permanent magnets or electrical excitation, reluctance machines, etc. These types can, in principle, be implemented either as radial flux or axial flux machines. The difference between radial and axial flux machines is illustrated in Figure 1.1. In the figure, the magnetic poles are indicated by red for north and blue for south. The arrows indicate the direction of the magnetic flux. The dark grey part is the rotor, and the light blue part is the stator.

In general, the vast majority of the electrical machines sold today are radial flux machines. Axial flux machines have, however, gained traction in recent years, and there are now several suppliers that sell axial flux machines [2][3][4]. The axial flux machine is especially compelling in cases where there is a high torque density demand and a low axial length-to-diameter ratio of the machine. There have been studies on inductance and reluctance machines, but the most popular machine today is the axial flux permanent magnet (AFPM) machine [1].

In [5], AFPM machines are compared to the conventional radial flux permanent

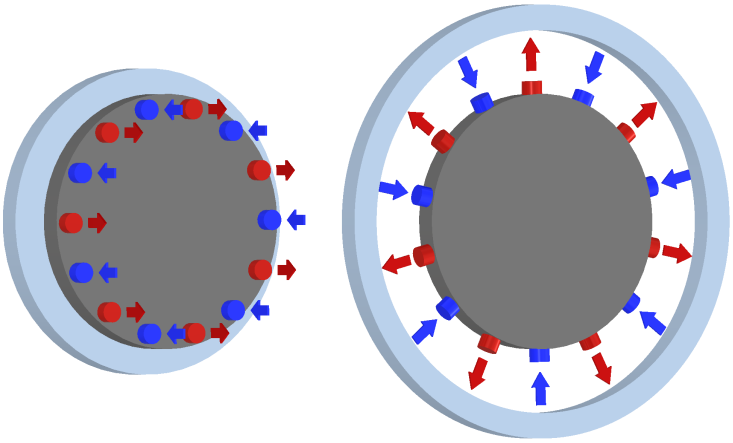

Figure 1.1: Visualization of the Difference Between the Flux in Axial (Left) and Radial (Right) Flux Machines

magnet (RFPM) machines. In this article, it can be seen that AFPM machines, for low axial length-to-diameter ratios, are more power dense than RFPM machines. The AFPM machine studied is composed of a single rotor and two stators, the latter referred to as the Kaman topology. The study points out that the AFPM machine is desirable for low length-to-diameter ratios, below 0.3, and with a higher number of poles [5].

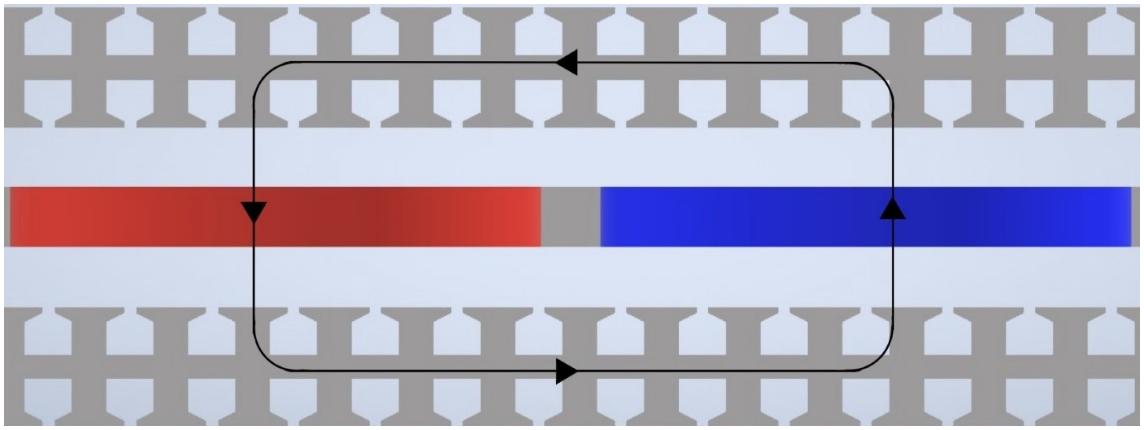

Figure 1.2: Kaman Topology, a Rotor Sandwiched Between Two Stators

The AFPM machines can be divided into four main groups: single stator single rotor (single-sided), double stator single rotor (Kaman type), single stator double rotor (Torus Type), and a multi-stack. The single sided machine is the simplest structure and both the Kaman and Torus type is derived from this type. If the Kaman or Torus types are stacked a multi-stack is achieved [6].

The Kaman type is a single rotor sandwiched between two stators. The main advantage of this topology is that it is possible to make the rotor coreless. This can be done since the main flux goes right through the rotor [7]. See Figure 1.2 for an illustration of the magnetic flux, where the red part marks permanent magnets'

north poles, blue marks the south poles, and the toothed part is the stator. Coreless refers to absence of magnetic material in the part that is coreless, the rotor for the Kaman topology. This means that the rotor can be made lighter, which gives less inertia [4][8]. Another advantage is that axial forces between the stator and rotor become very small due to the rotor being coreless.

The Torus topology is a single stator sandwiched between two rotors [7]. These rotors have two different magnetic configurations. North-to-North (NN) means that a magnet's north pole in one rotor points to the magnetic north of the corresponding magnet on the other rotor. Then there is the North-to-South (NS) configuration, where the north pole points towards the south pole of the other rotor. See Figure 1.3 for an illustration of the different magnetic configurations for Torus machines. The NS Torus machine has a magnetic field which does not travel in the hoop direction through the stator, meaning that it can be coreless. Instead, they have only windings, which are typically embedded in epoxy or similar material[4][8]. A negative aspect of the Torus machine is that it requires a core, or yoke, which transports the magnetic field in the rotor. A good material for this is steel, and an issue with it is that it is heavy, meaning larger inertia than the Kaman topology. It is, however, typically not necessary to use laminated steel. The rotor inertia of these machines becomes higher since there are two rotors as well, and each rotor also needs to contain steel/iron [8]. An advantage of the Torus topology is that when the rotors rotate, they also act like fans, dragging in new fluid to the stator windings, which transports away heat, i.e., cools the windings [7].

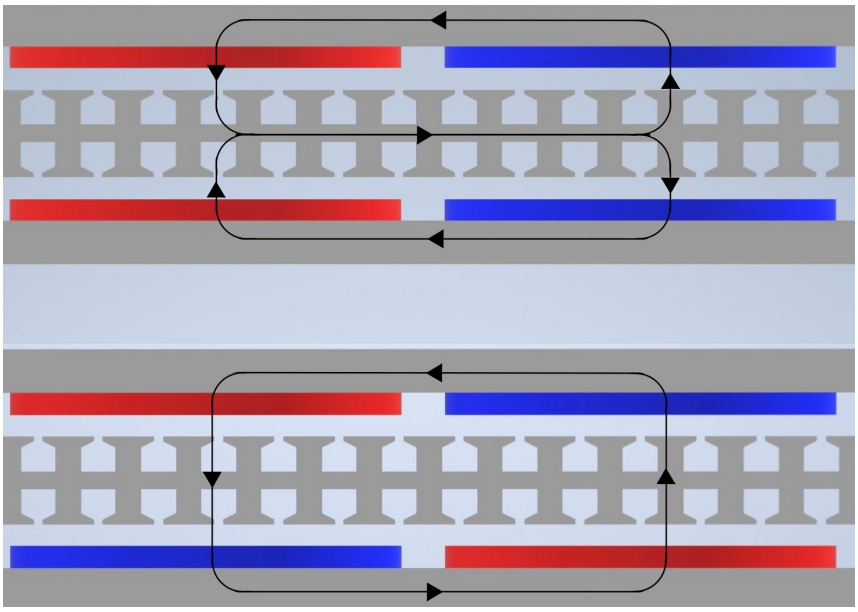

Figure 1.3: Torus topology, Single Stator Sandwiched Between Double Rotors with NN (Top) and NS (Bottom) Magnet Placement

A challenge with these machines is that there are strong magnetic forces involved which act on the rotor and the stator. This problem is less severe for coreless machines, where the axial forces are considerably smaller and do not fluctuate during

operation [6]. In [9], the issue with axial forces is solved for a single-sided AFPM by using a tapered roller bearing. An issue that can occur when using roller bearings in electrical machines is the risk of current-induced bearing damage due to electrical discharges at the metal surfaces [10]. This can significantly reduce the lifetime of the bearing, which leads to more frequent maintenance. Another issue that might occur is that since roller bearings are often made from magnetic steel, there is a risk that they become magnetized due to the magnetic field they are subjected to. Thereby, there is a risk that they attract debris from the surroundings, leading to erosion and a shorter lifespan of the bearings.

1.1.2 Bearings

Bearings are an excellent way of enabling relative movement between two solid surfaces while reducing wear and potentially carrying large loads. One type of bearing is the rolling element bearing. This bearing has surfaces with hard materials on the two separated bodies and rolling elements in between, which separate these surfaces. The rolling elements enable rotation with lower friction and lower wear, together with load carrying abilities through the solid material contacts [11]. Another group of bearings is the fluid bearing, where a fluid is used to separate the surfaces and where the fluid pressure carries the loads between the surfaces while maintaining separation. There are two main types of fluid bearings: hydrodynamic and hydrostatic.

The hydrodynamic bearing separates the sliding surfaces by the hydrodynamic pressure generated by the relative motion between the surfaces. Since the pressure is generated by the motion, there is no pressure to separate the surfaces when there is no motion or the motion is too slow. Since there is no motion at start and stop, there will be contact between the surfaces at those times and subsequent friction and wear on the surfaces. In situations where there is a lot of starting and stopping or low rotational speeds, it might not be beneficial for wear to use a hydrodynamic bearing. Hydrostatic bearings have an externally pressurized fluid that separates the surfaces. Externally pressurized fluid could therefore be beneficial in cases where the surfaces need to be separated at all times, independent of the rotational speed [12]. The bearing to be investigated is the hydrostatic bearing to be able able to maintain the seperations at all times.

1.2 Purpose and Objective

The purpose of this thesis is to do a comparative analysis of various configurations of a hydrostatic fluid bearing which is employed inside an electrical machine. The study aims to analyze different hydrostatic bearing designs with the help of Simcenter STAR-CCM+ (STAR-CCM+) and provide an assessment over the hydrodynamic losses, pressure distributions and risk of cavitation.

The objective for completing the project are as follows:

1. Build simulation models with good enough accuracy that calculates viscous friction near walls and pressure over the entire domain for different geometries.

   (a) Create the bearings' geometric design in CAD
   (b) Import and mesh CAD models in STAR-CCM+
   (c) Set up a continua that matches the fluid and flow conditions
   (d) Define and set boundary conditions for the model.
2. Use the simulation model to calculate performance parameters for a each of the designs.
3. Compare performance parameters between designs and choose the best suited geometry.

1.3 Limitations

In the actual machine, the rotor discs are subjected to magnetic forces and exhibit elastic behaviour. However, to simplify both the calculations and simulation setup, the discs are assumed to be rigid and magnetic forces are excluded from the analysis. This assumption allows for the use of conventional Computational Fluid Dynamics (CFD) methods, eliminating the need for Fluid-Structure Interaction (FSI) modelling.

Another simplification involves the use of geometric symmetry to reduce the simulation domain. By utilizing both rotational and plane symmetries, the domain is reduced to one sixth of its original size. This reduction significantly lowers the computational cost by decreasing the number of cells, thereby improving simulation speed and reducing storage required.

Constraints were also placed on geometry modifications for the bearing design. All modifications must comply with manufacturing and construction limitations, meaning that only changes feasible under the current production methods are permitted. Furthermore, it also means that any geometric alterations must be compatible with the existing structure of the electric motor, i.e, no changes in outer diameters of the stator.

Additional limitations is that the CFD simulation will be limited to STAR-CCM+ and no other CFD simulation software. On the hardware side, a maximum of 80 GB RAM was available, further limiting mesh resolution and model complexity depending on storage usage.

Due to confidentiality restrictions, results from all geometries based on Hagnesia's original pocket design can not be presented in visual content. The results from the geometries based on their configuration will instead be described in text. To visualize results, the Hagnesia geometry was simplified into a simpler geometric representation that will be used as a comparison and for visual content. The geometry used for the visual content is referred to as Basic or Basic geometry through out the report.

Not all simulations involve an imposed rotor tilt. Only the Basic geometry and the Hagnesia design were analysed under this condition. The simulations also excludes the gravitational components due to small dimensions deeming the gravitational effects negligible.

2
Theory

In the following chapter the theory of fluid dynamics, turbulence modelling, CFD, hydrostatic bearings, and some basic mechanics will be covered.

2.1 Solid Mechanics

When looking at solid mechanics the torque vector $\mathbf{M} = [M_x, M_y, M_z]^T$, where M_i is the torque around the i-axis, caused by a force, $\mathbf{F} = [F_x, F_y, F_z]^T$ acting in a point located at distance $\mathbf{r} = [x, y, z]^T$ from the $[0, 0, 0]$ point is then defined as follows:

$$\mathbf{M} = \begin{bmatrix} M_x \\ M_y \\ M_z \end{bmatrix} = \begin{bmatrix} F_z y - F_y z \\ F_x z - F_z x \\ F_y x - F_x y \end{bmatrix} = \mathbf{r} \times \mathbf{F} \tag{2.1}$$

If the torque vector is needed in a point located at an arbitrary point $\mathbf{X} = [X, Y, Z]^T$ while the force is located at point $\mathbf{x} = [x, y, z]^T$. Then to acquire the distance vector $\mathbf{r}$ simply subtract the coordinates for the force with the arbitrary points coordinates in which the torque vector wants to be acquired, i.e. use Eq. 2.1 but $\mathbf{r} = \mathbf{x} - \mathbf{X}$[13].

When having several different forces acting in different points and directions then the total torque around the $[0, 0, 0]$ point can be expressed by super position of all the individual forces contributions, meaning a torque sum is made of all torques created from each force. Eq. 2.2 shows the expression for the torque sum. The same can be done for the forces as well creating a force sum presented in Eq. 2.3

$$\mathbf{M}_{tot} = \sum_{i=1}^{n} \mathbf{M}_i = \sum_{i=1}^{n} \mathbf{r}_i \times \mathbf{F}_i \tag{2.2}$$

$$\mathbf{F}_{tot} = \sum_{i=1}^{n} \mathbf{F}_i \tag{2.3}$$

These sums can then be used to simplify a system of many forces and torques down to a single force vector and a single torque vector.

The forces on a body could come from different sources, one of which is friction. When a fluid passes over a solid surface a friction shear is created. The shear is always parallel to the surface. The shear vector $\boldsymbol{\tau}(\mathbf{x}) = [\tau_{xx}, \tau_{yy}, \tau_{zz}]$ is a function of the position and therefore varies over the area. The components of the shear vector is of the unit $\frac{N}{m^2}$ and can vary over the surface which is in contact with the fluid.

For an element with area dA so small that $\boldsymbol{\tau}$ can be considered constant over the surface, then the force vector for that element can be calculated as in Eq. 2.4.

$$\mathbf{dF}(\mathbf{x}) = \boldsymbol{\tau}(\mathbf{x})dA \tag{2.4}$$

Power can then be calculated as Eq. 2.5 shows:

$$P = Fv = M\omega \tag{2.5}$$

where v is the velocity in the same direction as the force and the angular velocity ω is around the same axis as the torque [13].

2.2 Fluid Dynamics

In fluid dynamics, the governing equations of fluid flow are mathematical representations of the fundamental conservation laws of physics. These laws include the conservation of mass, the principle that the sum of forces acting on a fluid particle equals the rate of change of momentum, and the principle that the rate of change of energy for a fluid particle equals the sum of the work done on the particle and the rate of heat added to the particle [14].

Before presenting any equations, it is necessary to introduce several variables. Pressure is denoted by P, and the velocity components in the x-, y-, and z-direction are represented by u, v, and w, respectively. These components are assembled into the velocity vector $\mathbf{u}$ as

$$\mathbf{u} = [u_x, u_y, u_z]^T = [u, v, w]^T \tag{2.6}$$

Dynamic viscosity is denoted by μ, and density by ρ. The terms S_{M_x}, S_{M_y}, and S_{M_z} represent source terms for the momentum equations in the x-, y-, and z-direction, respectively, and include only contributions due to body forces. In cases where gravity acts in the z-direction, the only non-zero term is $S_{M_z} = -\rho g$ [14].

Then there is the divergence operator which is defined as $div(\phi) = \nabla \cdot \phi = \frac{\partial \phi_k}{\partial x_k}$ and last but not least the gradient operator defined as $grad(\phi) = \nabla\phi = \frac{\partial \phi}{\partial x_k}\hat{\mathrm{e}}_k$[15][16]. With these definitions established, the expression for the conservation of mass can be introduced as shown in Eq. 2.7.

$$\frac{\partial \rho}{\partial t} + \rho\frac{\partial u_i}{\partial x_i} = 0 \tag{2.7}$$

Before addressing the momentum equations, the concept of a Newtonian fluid must be understood. A Newtonian fluid is characterized by viscous stresses that proportionally varies with the dynamic viscosity and the rate of strain of fluid elements. An expression describing this stress variation is provided in Eq. 2.8. The second part of the equation involves a second viscosity, λ, about which little is known. However, for incompressible flows, the continuity condition makes the second viscosity term equal to zero, meaning it vanishes from the equaiton [14][17]. The symbol δ_{ij} represents the Kronecker delta, which equals one when $i = j$ and zero otherwise [16].

$$\tau_{ij} = \mu\left(\frac{\partial u_i}{\partial x_j} + \frac{\partial u_j}{\partial x_i}\right) + \underbrace{\lambda\frac{\partial u_k}{\partial x_k}\delta_{ij}}_{incompressible \implies =0} \tag{2.8}$$

By relating shear stresses to velocity derivatives and substituting these into the momentum equations, the Navier–Stokes equations are obtained. These equations provide one expression for each of the x-, y-, and z-direction and are presented in Eq. 2.9[14].

$$i\text{-direction}: \quad \frac{\partial \rho u_i}{\partial t} + \rho\frac{\partial u_i u_j}{\partial x_j} = -\frac{\partial P}{\partial x_i} + \mu\frac{\partial^2 u_i}{\partial x_j \partial x_i} + S_{M_i} \tag{2.9}$$

When solving for incompressible flows it is common to use the hydrodynamic pressure p instead of the pressure P. This term excludes the ambient pressure and the gravity component. The hydrodynamic pressure is also equal to zero when the velocity field is equal to zero. Using the hydrodynamic pressure and inserting it into Eq. 2.9 then give the Eq. 2.10 where the pressure now instead is the hydrodynamic pressure [18].

$$i\text{-direction}: \quad \frac{\partial \rho u_i}{\partial t} + \rho\frac{\partial u_i u_j}{\partial x_j} = -\frac{\partial p}{\partial x_i} + \mu\frac{\partial^2 u_i}{\partial x_j \partial x_i} \tag{2.10}$$

Additionally, the energy equation describes the rate of change of energy for a fluid particle as the sum of the rate of heat added and the mechanical work done on the particle. This equation is presented in Eq. 2.11, where i denotes internal (thermal) energy, Φ is the viscous dissipation function, and S_I represents a source term. Definitions of the dissipation function and source term can be found in [14].

$$\frac{\partial \rho i}{\partial t} + div(\rho i \mathbf{u}) = -p\,div(\mathbf{u}) + div(k\,grad(T)) + \Phi + S_i \tag{2.11}$$

Now there is an equation system of five equations with seven unknowns: u, v, w, p, i, T, and ρ. This means that, for the system to be mathematically closed, two additional equations are required, which can be retrieved by using equations of state for the fluid. For a perfect gas, for instance, the equations $p = \rho RT$ and $i = C_v T$ can be used to relate these variables to each other, giving seven equations and therefore closing the system and making it solvable. Liquids, on the other hand, are considered to be incompressible, meaning no change in density [14].

Fluids that are considered to be incompressible have no variation in density. No density variation means that the solution can be retrieved using only the conservation of mass and the Navier–Stokes equations, unless heat transfer needs to be included. This can be done since the conservation of mass and Navier–Stokes equations make up four equations with the four variables u, v, w, and p, now deeming it solvable [17].

To solve these equations some initial boundary conditions are needed and then an iterative algorithm iterates over the domain to solve for the variables. The boundary conditions could include an inlet velocity, inlet pressure, an outlet pressure, or a wall

condition implying having the same velocity in the same direction as the wall at the wall. Boundary conditions can also be applied in the form of wall shear stress [18].

2.2.1 Turbulence

When performing fluid dynamic calculations, the flow may be either laminar or turbulent. A common rule of thumb to determine whether the flow is turbulent is to calculate the Reynolds number, Re. This quantity is given by

$$Re = \frac{\rho U d}{\mu} \tag{2.12}$$

where U is the fluid velocity and d is the characteristic length. Generally, for flow in a pipe, if $Re < 2300$, or for boundary layer flows over flat plates, if $Re < 10^6$, the flow can be considered laminar which is characterized by smooth and steady motion. If Re exceeds these thresholds, the flow is considered to transition or become turbulent [17].

Turbulent flow lacks a strict definition but possesses identifiable characteristics. It is chaotic, irregular, three-dimensional, and unsteady. Turbulent flows displays a spectrum of eddy sizes, known as scales. Although a precise definition of a turbulent eddy is not established, it is commonly described as a structure that exists within a specific spatial region for a finite duration before dissipating through the cascade process or dissipation. Turbulent eddies are defined by distinct velocity and length scales. Larger eddies may contain smaller eddies, and the largest eddies typically correspond to the size of the flow geometry, such as the boundary layer thickness or the width of a jet. At the opposite end of the spectrum, the smallest eddies are dissipated by viscous forces, converting kinetic energy into thermal energy and increasing the fluid temperature [18].

Despite the flow being chaotic, turbulence remains deterministic and is governed by the Navier–Stokes equations. Diffusivity for turbulent flow is greater than for laminar flow, resulting in enhanced heat transfer and increased wall friction in internal flows such as channels. Additionally, turbulent flows are dissipative. The dissipation of the smallest eddies leads to the conversion of kinetic energy into thermal energy, contributing to a rise in fluid temperature [18].

In turbulent flow analysis, it is advantageous to decompose instantaneous variables into a mean, time averaged, component and a fluctuating component. This decomposition for pressure and velocity are expressed as:

$$p = \bar{p} + p' \,, \quad u_i = \bar{u}_i + u_i' \tag{2.13}$$

where $\bar{\cdot}$ denotes the time averaged component and $\cdot'$ denotes the fluctuating component. The pressure p in this context refers to the hydrodynamic pressure, implying that when the mean flow velocity field is zero, the pressure is also zero [18]. This decomposition is used because resolving all turbulent scales requires extremely fine computational grids and small time steps. It is also usually the mean flow quantities

that is of interest in many practical applications [19]. The time averaged part for a variable ϕ is defined as

$$\bar{\phi} = \frac{1}{2T}\int_{-T}^{T} \phi \; dt \tag{2.14}$$

Time averaging the mean part equals itself since $\bar{\cdot}$ is independent of the time and therefore can be moved outside the integral resulting in:

$$\bar{\bar{\phi}} = \frac{1}{2T}\int_{-T}^{T} \bar{\phi} \; dt = \frac{\bar{\phi}}{2T}\int_{-T}^{T} 1 \; dt = \frac{\bar{\phi}}{2T} 2T = \bar{\phi} \tag{2.15}$$

This in turn leaves that $\bar{\phi'} = 0$ since

$$\bar{\phi} = \frac{1}{2T}\int_{-T}^{T} \phi \; dt = \frac{1}{2T}\int_{-T}^{T} \underbrace{\bar{\phi} + \phi'}_{=\phi} \; dt = \underbrace{\bar{\bar{\phi}}}_{\bar{\phi}} + \bar{\phi'} \implies \bar{\phi'} = 0 \tag{2.16}$$

Applying this decomposition to the velocity and pressure fields and substituting into the Navier Stokes equations leads to the Reynolds Averaged Navier Stokes (RANS) equations, as shown in Eq. 2.17 [18].

$$\rho \frac{\partial \bar{u}_i \bar{u}_j}{\partial x_j} = -\frac{\partial \bar{p}}{\partial x_i} + \frac{\partial}{\partial x_j}\left(\mu \frac{\partial \bar{u}_i}{\partial x_j} - \rho \overline{u_i' u_j'}\right) \tag{2.17}$$

The final term in the RANS equations, $-\rho\overline{u_i' u_j'}$, depends entirely on the fluctuating velocity components and forms a symmetric stress tensor known as the Reynolds stress tensor. This Reynolds stress term represents the effects of turbulence and introduces six additional unknowns. Combined with the three velocity components and the pressure, there are now ten unknowns in total, but only four governing equations: the RANS equations and the continuity equation. To solve this system, a closure model is required [18].

2.2.2 Closure Models

Various modelling approaches are employed to close the system of equations in turbulent flow analysis. A common type of model is the eddy viscosity models. These models utilizes the turbulent viscosity, also known as eddy viscosity, together with the Boussinesq assumption to express the Reynolds stresses in terms of eddy viscosity, mean flow velocity gradients, and the turbulent kinetic energy. The application of the Boussinesq assumption to the Reynolds stresses is illustrated in Eq. 2.18 [18][19].

$$\overline{u_i' u_j'} = -\nu_t \left(\frac{\partial \overline{u}_i}{\partial x_j} + \frac{\partial \overline{u}_j}{\partial x_i}\right) + \frac{2}{3} k \delta_{ij} \; , \quad k = \frac{\overline{u_i' u_i'}}{2} \; , \quad \nu_t = \frac{\mu_t}{\rho} \tag{2.18}$$

Models that use eddy viscosity are commonly referred to as eddy viscosity models. One of the simplest eddy viscosity models is the algebraic models, which utilizes algebraic expressions to estimate the turbulent viscosity, μ_t, also known as eddy viscosity [19].

An alternative approach is the one-equation models, in which a single transport equation is formulated for one turbulent quantity, while a second is derived using an algebraic expression. However, this model faces challenges because there is no universally applicable algebraic expression for quantities like the turbulence length scale in general flows. Although computationally less expensive, one-equation models typically shows reduced accuracy compared to two-equation models when it comes to modelling the turbulence [19].

A more accurate choice compared to the one-equation models is the two-equation models. These models falls under the eddy viscosity models and they derive two transport equations for scalar quantities for example turbulent kinetic energy, k, and turbulent dissipation rate, ϵ. These two scalar quantities are then used to determine the eddy viscosity [19].

A third model type, which is not a eddy viscosity model, is Reynolds Stress Models (RSM), which formulate transport equations directly for each component of the Reynolds stress tensor, $\overline{u_i' u_j'}$, along with a turbulent scalar, typically ϵ. These models offer the advantage of capturing the effects of streamline curvature, which can amplify or dampen turbulence. However, their complexity, high computational cost, and numerical instability, primarily due to small second-order stabilizing terms in the momentum equations pose significant challenges [19].

Two widely used eddy viscosity models are the k–ϵ and k–ω models. The k–ϵ model is among the most commonly implemented two-equation models. It solves transport equations for k and ϵ, which are then used to compute the turbulent viscosity [20]. The k–ω model also solves the k equation but replaces ϵ with the specific dissipation rate, ω [19].

One significant drawback of the k–ϵ model is the development of numerical issues in regions where turbulence intensity is low, such as in the viscous sublayer. This is because the ϵ equation contains a $\frac{\epsilon^2}{k}$ term, where ϵ and k do not decrease at the same rate, leading to instabilities. The k–ω model avoids this problem, as ω smoothly approaches zero with k, making it suitable for near-wall modelling [19]. Additional limitations of the k–ϵ model include the need for fine grid resolution near walls and reduced accuracy in flows with adverse pressure gradients [20].

The SST k–ω was developed to combine the strengths of both the k–ϵ and k–ω models. This model uses the k–ω formulation in regions where it performs well, such as the viscous sublayer, logarithmic boundary layer under adverse pressure gradients, and compressible flows. It then switches to the k–ϵ formulation in regions where it offers advantages, such as wake regions and free shear layers. A known limitation of the SST k–ω model is the requirement for explicit knowledge of the distance to the nearest wall [20].

For the SST $k-\omega$ model the boundary conditions at solid walls for k and ω is:

$$k = 0, \quad \omega = 10\frac{6\mu_L}{\rho\beta_1(d_1)^2} \tag{2.19}$$

where μ_L is the laminar dynamic viscosity, d_1 is the distance from the centroid of the first computational cell to the wall, and $\beta_1 = 0.75$. A normalized wall distance of $y^+ < 3$ is required for the application of this boundary condition [20]. Additional details on turbulence models and their corresponding equations, as well as treatment of boundary conditions, and how the normalized wall distance is defined can be found in [18] and [20].

2.2.3 Vapour Pressure

When working with liquids, it is important to consider the vapour pressure. Vapour pressure, p_v, is the pressure at which a liquid boils, i.e. transitions from a liquid state to a gaseous state. As long as the vapour pressure is lower than the pressure of the liquid it will remain in its liquid phase, and the only exchange between liquid and vapour is evaporation at the interface. The vapour pressure also varies with the temperature of the liquid. For example, water at 20 °C has a vapour pressure of 2.340 kPa, while at 100 °C, the vapour pressure is 101.3 kPa. When a flow phenomenon causes the pressure of the liquid to drop below the vapour pressure, vapour forms within the liquid, a process known as cavitation. One problem associated with cavitation is that the collapse of vapour bubbles can cause erosion of the material in contact with the fluid. Cavitation therefore leads to increased wear, causing components to degrade more rapidly. Consequently, it is important to ensure that the liquid pressure remains above the vapour pressure at all temperatures the liquid might have during a working cycle to minimize surface wear to extend the lifespan of components in contact with the liquid [17][21].

2.3 CFD

In CFD simulations, various options and settings must be considered. This section outlines some of the fundamental theory necessary for selecting meshing strategies and simulation configurations.

2.3.1 Fluid Flow

When using STAR-CCM+, different fluid flow models are available, each solving the governing equations in a distinct manner. The first is the "Segregated Flow" model, which solves the momentum equations sequentially. In this approach, each directional momentum equation is solved independently, with coupling achieved through a pressure correction equation. This equation ensures that the resulting velocity field satisfies the mass conservation constraint and is derived from the continuity and momentum equations. STAR-CCM+ offers two pressure-correction coupling algorithms: SIMPLE and PISO. The SIMPLE algorithm is well-suited for simulations using larger time steps, while the PISO algorithm is more appropriate when taking smaller time steps. Segregated solvers are typically used for constant density flows and can handle mildly compressible flows or flows with low Rayleigh numbers. For applications involving shocks, high Mach numbers, or high Rayleigh numbers, the

segregated solver is not appropriate and in such cases a "Coupled Flow" model is recommended [22].

The "Coupled Flow" model uses a pseudo-time-marching method to solve the momentum and continuity equations simultaneously instead of doing it sequentially like the segregated does. This model performs well for flows with dominant source terms and maintains good convergence behaviour even when the mesh is refined, as CPU time scales linearly with the number of cells. However, a drawback of this method is its higher memory consumption, as multiple equations must be solved simultaneously for each cell [22].

Another thing to keep in mind is the turbulence specification in STAR-CCM+. This setting controls how the turbulence profile within a porous region, at flow boundaries, and for initialization is defined. When the velocity field is unknown and set to zero at the beginning of the simulation this method needs to be set to "$k + \epsilon$" or "$k + \omega$" for the corresponding turbulence closure models [22].

2.3.2 Meshing

Mesh generation involves several factors, including desired convergence rate, solution accuracy, whether a single- or multi-region mesh is used, the quality of the initial surface mesh, geometry thickness, available memory, and mesh generation time. Each mesh type has its own advantages and disadvantages, and these considerations may not be compatible. For example, a tetrahedral mesh requires the least time and memory per generated cell. However, it requires five to eight times the amount of cells compared to a polyhedral or trimmed cell mesh to reach the same accuracy in the simulation results. This can then potentially offset the time savings due to longer convergence times [22].

"Prism Layer Mesher" may also be used to generate layers of cells with ascending thickness from a surface and outward. The total thickness and the number of layers can be defined together with a growth speed, resulting in a fine mesh near the wall. The smallest cell is positioned closest to the wall, while the largest is at the outer boundary of the prism layer. This technique helps apply boundary conditions accurately for turbulence models by keeping the y^+ values low close to the walls [22].

2.3.3 Periodicity

For flows where periodic behaviours can be defined, a fully developed interface must be defined for the periodic surfaces. A pressure drop or mass flow rate over the interface surfaces (in the case of the segregated flow model) is then defined. This boundary condition can be configured as either translational periodicity, rotational periodicity, or both, depending on the nature of the symmetry [22].

2.4 Fluid Bearings

In rotating systems, bearings are typically used to minimize friction and wear. Bearings are generally categorized as rolling element bearings or sliding/journal bearings. Rolling element bearings utilize elements such as balls, rollers, or needles to support loads while minimizing friction between the surfaces of the components in relative movement [23]. These elements are typically metallic, although alternative materials such as ceramics may be used but are more expensive than the metal. In environments involving magnetic fields or electrical machinery, metal bearings may introduce current and magnetism related issues, as noted in Section 1.1.2 [24]. Suitable alternatives for the bearings in this can be journal bearings.

Journal bearings function by maintaining a thin or thick fluid film between the bearing surfaces. This film reduces both friction and wear while supporting loads through fluid pressure [23]. A type of journal bearing that offers effective load support is the hydrostatic bearing.

The hydrostatic bearing maintains complete separation between surfaces via an externally pressurized fluid film. As the fluid is pressurised externally, separation is maintained even when movement is not present. This is a key distinction from hydrodynamic bearings, which rely on motion to establish fluid pressure that separates the surfaces. Since motion is required for separation of the surfaces this means that they become subject to wear during startup and shutdown. Depending on the working fluid, hydrostatic bearings may be referred to as aerostatic (gas) or hydrostatic (liquid), but are often referred to with the collective term externally pressurized bearings [25].

A typical hydrostatic bearing consists of a thin gap between surfaces, with a recess pocket embedded in one surface. The pocket is significantly deeper than the gap and induces flow resistance. Pressurized fluid enters the pocket through a restricting orifice and exits via the narrow gap between the bearing land and the opposing surface. As the fluid passes over the lands, its pressure drops, and upon exiting the edge, it returns to ambient pressure [25]. A schematic representation is shown in Figure 2.1.

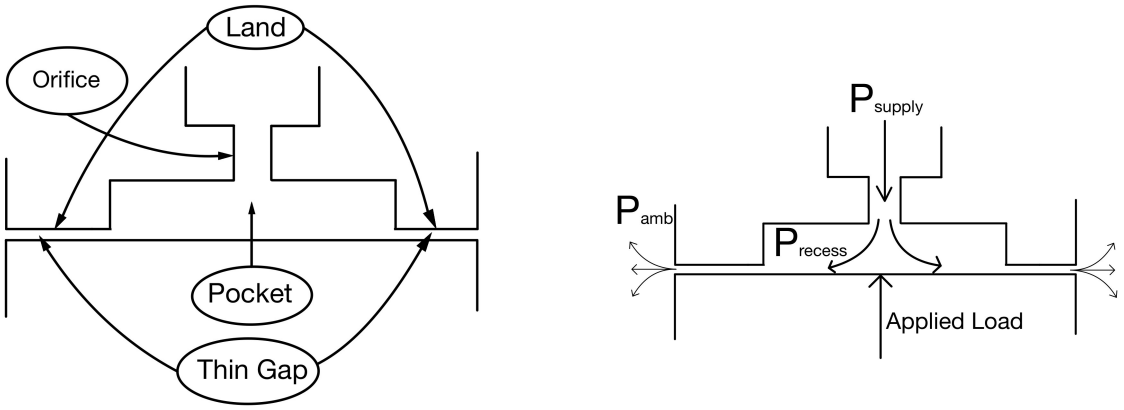

Figure 2.1: Explanation and Visualization of a Hydrostatic Bearing

The pressure distribution within the gap and over the lands supports the applied load. If the load varies, the pressure in the recess pocket must also change. For this to occur, the condition $P_{\text{recess}} < P_{\text{supply}}$ must be met under intended loading. The maximum load capacity corresponds to the point at which the recess pressure equals the supply pressure. As the load increases, the pressure drop across the orifice decreases, while the pressure drop across the lands increases, reducing the gap width. When the maximum load carried the pressure in the recess pockets reaches the supply pressure. When the load is removed, the recess pocket pressure approaches ambient pressure, increasing the pressure drop over the restricting orifice and reducing the pressure drop over the lands causing the gap to expand until the only significant pressure drop occurs across the restricting orifice [25].

3
Methods

In this chapter the method which was employed to reach the results is described together with motivations to why some of the choices are made.

3.1 Machine Specifications

The electrical machine that is to be evaluated is a motor optimized to be used for ship propulsion. The expected operating speed is 500 RPM which corresponds to approximately 52.36 Radians per second. The inner and outer radius of the circular rotor disc is 113.8 mm and 190 mm respectively. A maximum velocity of approximately $10\frac{m}{s}$ is then received at the outer edge off the disc, using the relation $v = r\omega$. The thickness of the gap between the rotor and the stator is 0.04 mm. The depth of the pockets on the stator is 0.142 mm, which means a total distance of 0.182 mm between the rotor and the stator. Using these values and calculating the Reynolds number gives a number that varies between 110 and 825 in the fluid gap. The expected fluid velocity at the inlet to the slits from the manifold is not known. The oil delivery pump increases the total pressure of the fluid with four bar and the ambient fluid pressure is two bar. The expected power delivery of one machine operating at 500 RPM is 458.15 kW [4].

VG2 oil is used as fluid for the bearing. The VG2 oil has a density of $\rho = 790\frac{kg}{m^3}$ and a midpoint kinematic viscosity of 2.2 centi Stokes (cSt) at a temperature of 40 ^{o}C [26]. 2.2 cSt corresponds to a dynamic viscosity of $1.738 \cdot 10^3 Pa \cdot s$. No data could be found of the VG2 oils vapour pressure but a similar lubricant with approximately the same density and viscosity is the Mobil Velocite Oil No. 3 with a vapour pressure below one mmHg, at 20 ^{o}C [27]. Converting from mmHg to Pa gives a vapour pressure below 134 Pa. As a safety precaution the vapour pressure will therefore be assumed to be 134 Pa.

3.2 Geometry

The company provided 3D CAD models of all the parts of the electric machine. The part of interests, the stator block, was isolated and opened up in Autodesk Inventor to be edited. The part was symmetric around the middle plane in the axial direction so one half was removed. This was done by extruding the outer geometry as a cut up to the symmetry plane. The model provided was only of the part of the stator where the pockets are located which does not reach the full 120 ^{o} that is needed

for the symmetry. An extension of the geometry was therefore made, equally on both sides of the given stator model, to reach the desired 120 ^{o}. The gap between the stator and rotor in the extension areas is 0.02 mm wider as well. When doing simulations in STAR-CCM+ the desired 3D model to import is the fluid volume. The CAD model provided by Hagnesia was of the solid volume of the stator, where there were gaps where the fluid should be, like the part to the left in Figure 3.1 of an example geometry. These gaps were internal of the solid volume provided but also external, representing the gap between the stator and rotor, like the picture to the right in Figure 3.1. This gap is 0.04 mm wide over the pocket area and 0.06 mm in the extensions made. The CAD models therefore needed to be modified so that the gap areas where the fluid should flow needed to be the part volume while the solid parts was removed and represented by the empty space. This was done by making a new solid that was made of both the the fluid and the solid volumes, the middle picture of Figure 3.1. Inventor has a function called "Combine" that then was used to cut out the provided solid volumes from the new solid part created. This left behind only the fluid volumes and removed the solid volumes.

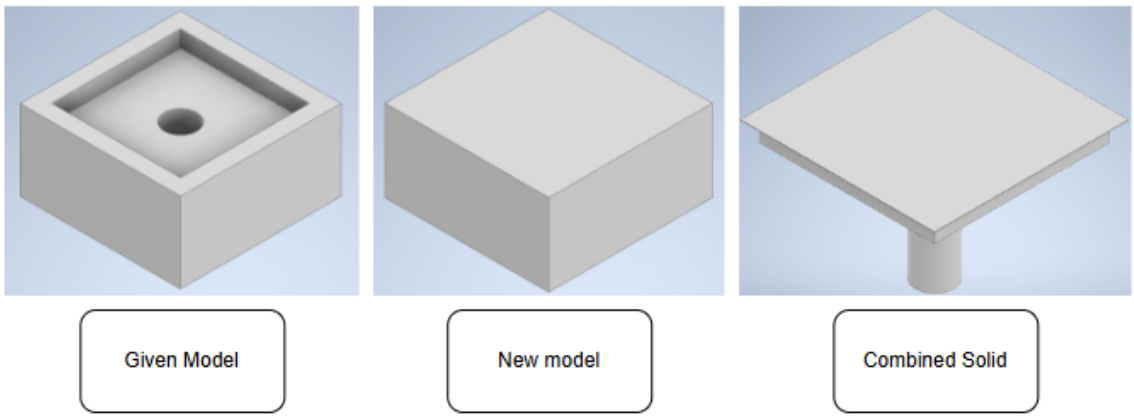

Figure 3.1: Example of the given solid volume model (Left), COmbined Solid and Fluid Bolume part (Middle), and Fluid Volume Given From the Solid (Right)

The simulations were conducted for multiple geometric configurations. The tested geometries are as follows: the first is the Original geometry, provided by Hagnesia AB. The second configuration is based on the Original geometry but with the depth of the fluid recess pockets reduced to half. The shallower pocket geometry will be referred to as the Shallow geometry. The third configuration involves the addition of a fillet radius to the inner corner of the recess pockets in the solid volume of the Original geometry. For clarification, the location of the filleted corner on the solid volume is shown in Figure 3.2 and a pocket in fluid volumes that has been filleted can be seen in Figure 3.3.

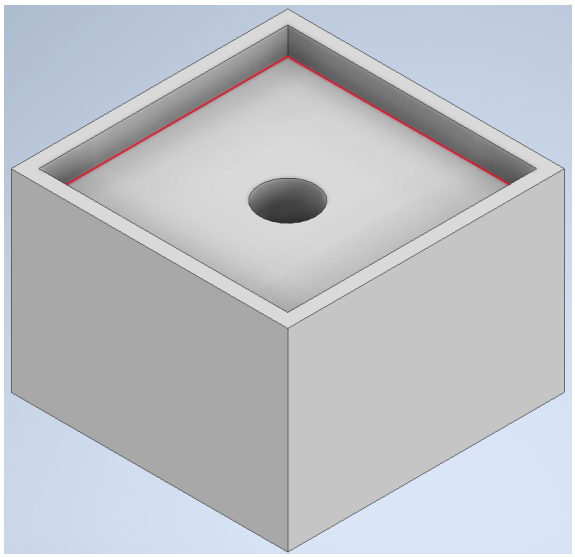

Figure 3.2: Marking of Filleted Corner on the Example Model of the Given Solid CAD Model

The inner corner of the recess pockets was filleted with a radius that is large relative to the pocket depth to smooth out the transition in to the pocket. The reason the inner corner is filleted instead of the outer corner is due to manufacturing constraints. Two different filleted geometries were created: one with a 2 mm fillet and another with a 5 mm fillet. A view of the 5 mm filleted pocket in the fluid domain is shown in Figure 3.3.

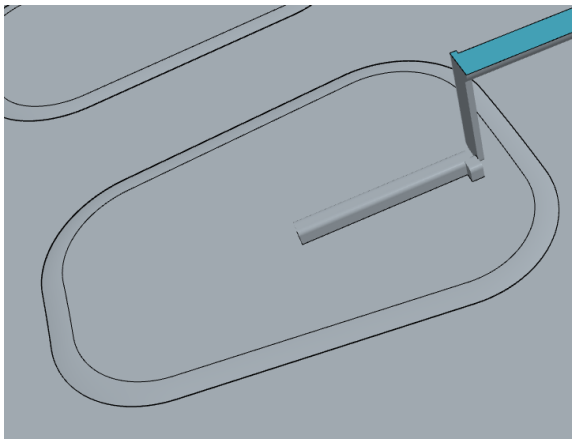

Figure 3.3: Pocket With Filleted Edges for the Fluid Domain

In addition, a geometry was created with half the number of recess pockets compared to the Original geometry. This configuration is referred to as the Basic geometry. All of the geometries were simulated in an equilibrated state, meaning that the magnetic forces from the stators on either side of the disc are assumed to be equal, resulting in no deflection of the rotor. Throughout this report, this condition will be referred to as the equilibrated state or as the disc being in equilibrium.

Both the Original and Basic geometry were further modified to include an imposed

rotor tilt. This was achieved by linearly increasing or decreasing the fluid gap between the rotor and stator from the inner radius to the outer radius. The geometry with a decreasing gap thickness is referred to as the thinner gap configuration, while the one with an increasing gap is called the thicker gap. The outer edges gap thickness was 0.02 mm thinner or thicker. This imposed deflection was mentioned as a desired maximum allowed deflection by Hagnesia. An illustration of the increasing gap from inner to outer radius is provided in Figure 3.4. The dashed red line is the fluid films geometry before it was made thinner or thicker. The reason for doing this is to see how the pressure distribution is affected by a deflection of the rotor and how the bearing will try to oppose this deflection pushing the rotor back in to place.

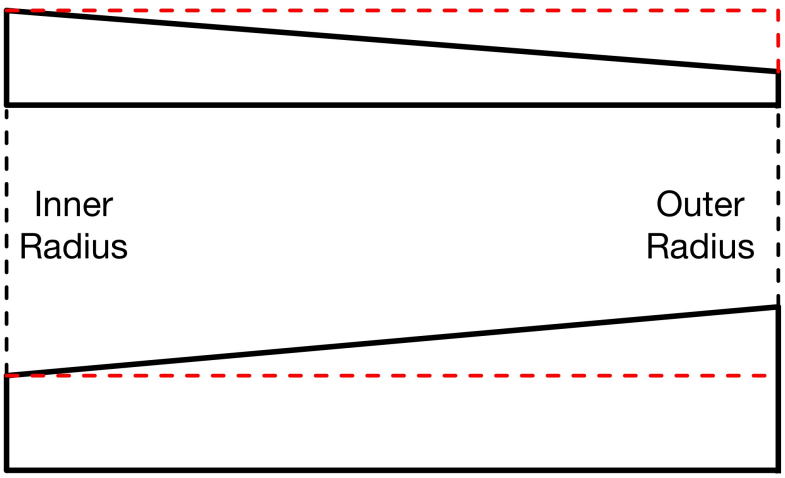

Figure 3.4: How the Fluid Gap Thickness Varies in the Radial Direction for a Thinner (Top) and Thicker (Bottom) Gap

Once completed, all geometries were exported to .x_t format for import into STAR-CCM+. A complete view of the fluid volume for the Basic geometry can be seen below in Figure 3.5.

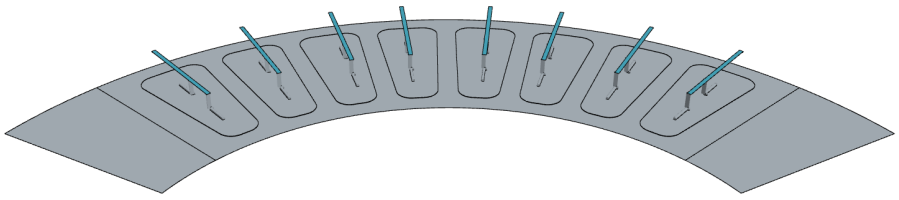

Figure 3.5: Complete View of the Full Fluid Domain for the Basic Geometry

After export, the geometries were imported into STAR-CCM+ as surface meshes with tessellation density set to "Very Fine". Within STAR-CCM+'s 3D-CAD environment, additional modifications were made. The modification was the rotor surface being split along the contours of the recess pockets and the edge where extension start, i.e. the gap widens between the rotor and stator. This was accomplished using the "Split Faces By Edge Projection" function in the 3D model module of

STAR-CCM+. The rotor surface was selected as the face to be split, and the edges of the pockets and the outer edge of the stator disc with the pocket geometry were selected. The selected edges, shown as blue lines in Figure 3.6, were projected in the negative z-direction and cut on the rotor surface, the red surface.

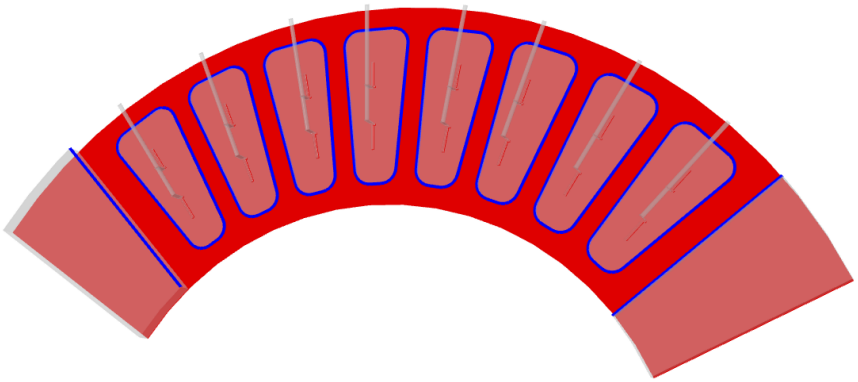

Figure 3.6: Split by Edge Projection Clarification

The part's surface was divided into different surface groups by the use of "Divide by Patch". Figures 3.7 to 3.9 shows the various surface regions. The blue surfaces in Figure 3.7 corresponds to the "Manifold Sym" surface, which represents a symmetry boundary. The large magenta colored area indicates the "Lands" surface, corresponding to the bearing lands region of the stator. The smaller magenta blocks are the "Slits" surfaces. The smaller grey regions represent the recess pockets and are labelled "Pocket Bottom". The surfaces connecting the "Lands" and "Pocket Bottom" is the "Pocket Sides" surfaces. The larger grey regions near the edges are the "Ext Upper Wall". Between the "Ext Upper Wall" and the "Lands" surfaces are two thin vertical surfaces named "Ext Vert Wall". Lastly, the grey tube like structure connected to both the blue surface and the "Slits" is referred to as the "Manifolds". All these surfaces are modelled as stationary walls except for the "Manifold Sym" which is modelled as a symmetry.

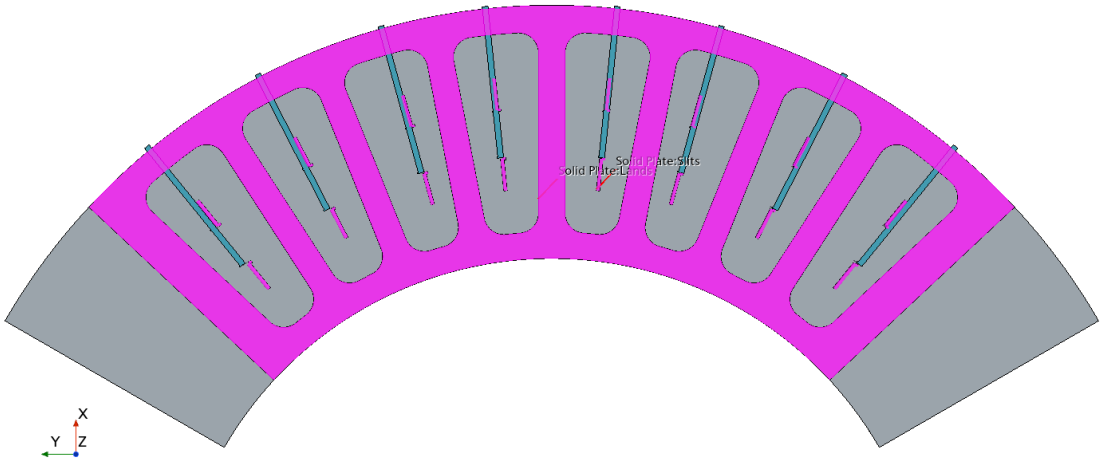

Figure 3.7: Surfaces on the Stator Segment of the Domain

In Figure 3.8, the entire rotor surface is shown. The magenta coloured region represent the bearing lands on the rotor, labelled "Rotor Lands". The grey areas with rounded corners are identified as the "Rotor Pocket" surface, while the larger grey regions correspond to "Rotor Ext". As the rotor is in a rotating motion, these surfaces are modelled as walls with a rotational tangential velocity of 52.36 rad/s (approximately 500 RPM) around the z-axis.

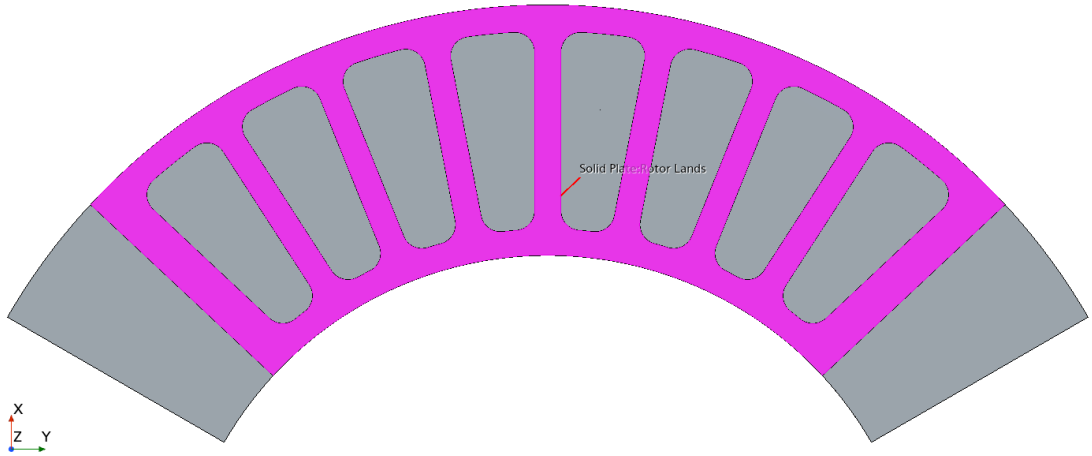

Figure 3.8: Surfaces on the Rotor

Last is Figure 3.9. If looking at the figure the remaining surfaces is marked with the corresponding name. The name is the part written after "Solid Plate:". For clarification the "Outlet Inner" and "Outlet Outer" is the surface with normals in the radial direction, where the inner is located at the inner radius of the section. The "Inlets" is the inlets to the manifolds and the IF surfaces is the periodic surfaces with normals in the circumferential direction. Once all the surfaces were divided a region was created with one region for each part and one boundary for each surface.

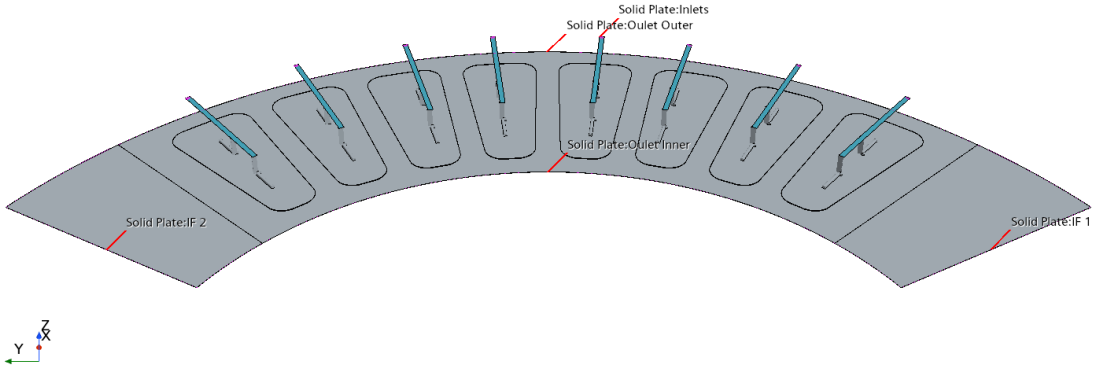

Figure 3.9: Outlets, Inlets and IF Surfaces

3.3 Mesh

The mesh was generated using the STAR-CCM+ automated mesh tool. The "Surface Remesher" was used in combination with the "Trimmed Cell Mesher" and the "Prism Layer Mesher". The mesher was configured to run in parallel, enabling meshing across multiple cores to reduce meshing time. Under "Default Controls", several settings were modified and these settings and their corresponding values are presented in Table 3.1.

Table 3.1: Default Controls for Meshing

Control	Value
Base Size	0.35 mm
Minimum Surface Size (Relative to base)	100 %
Surface Growth Rate	Slow
Number of Prism Layers	8
Gap Fill Percentage	45
Minimum Thickness Percentage	1.0
Prism Layer Total Thickness (Absolute)	0.072 mm

Certain surfaces required custom mesh controls to improve mesh quality. These control settings and their associated surfaces are provided in Table 3.2.

Table 3.2: Surface Controls for Different Surfaces

Surfaces	Control	Value
IF 1, IF 2, Inlet Manifold Sym, Outlet Inner, Outlet Outer	Prism Layer	Disable
Lands, Rotor Lands	Number of Prism Layers	6
	Prism Layer Total Thickness	0.0165 mm
Manifold	Target Surface Size	0.08 mm
	Minimum Surface Size	0.033 mm
	Trimmer Surface Growth Rate	Very Slow
Pocket Sides, Ext Vert Wall	Target Surface Size	0.05 mm
	Minimum Surface Size	0.01 mm
Slits	Target Surface Size	0.05 mm
	Minimum Surface Size	0.05 mm
	Trimmer Surface Growth Rate	Very Slow

To determine suitable mesh settings, a simplified version of the domain was created, comprising only a single pocket as shown in Figure 3.10. This was done to accelerate meshing and simulation times. A mesh was then generated for this simplified

geometry and a simulation of the section was conducted to assess convergence behaviour and evaluate normalized wall distances, y^+. This verification ensured that the boundary conditions were compatible with the low y^+ treatment, i.e., $y^+ < 3$, on the majority of the domain surfaces.

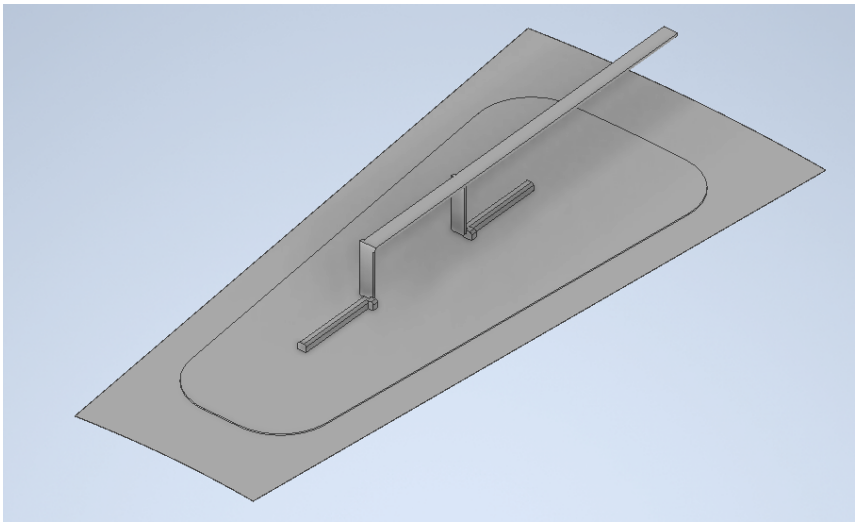

Figure 3.10: Section Piece Used for Finding Mesh Parameters

For the other geometries some of the mentioned settings was changed to reach an acceptable mesh. In Table 3.3 it is possible to see what settings what were changed for each geometry.

Table 3.3: Mesh Settings Changes for Other Geometries

Model	Region	Control	Value
Shallow	Pocket Sides,ExtVertWall	Target Size	0.033 mm
2 mm Fillet	Default Controls	Surface Growth Rate	Default
5 mm Fillet	Default Controls	Surface Growth Rate	Default
	Pocket Sides/ExtVertWall	Surface Growth Rate	0.06 mm
	Pocket Sides/ExtVertWall	Minimum Surface Size	0.05 mm
Thick Gap	Rotor Lands, Lands	Prism Layer Total Thickness	0.0215 mm
	Rotor Lands, Lands	Number of Prism Layer	7
Basic Thick Gap	Rotor Lands, Lands	Prism Layer Total Thickness	0.0215 mm
	Rotor Lands, Lands	Number of Prism Layer	7

3.4 Simulation

Once the mesh was completed, the next step involved setting up the fluid simulation. The flow was modelled as an incompressible liquid with a viscous regime set to turbulent. The SST k–ω turbulence model was selected. Although the Reynolds number for the system is not high enough to definitively classify the flow as turbulent, a turbulent flow regime was still assumed. This decision is based on the potential for turbulence to arise from geometric irregularities and from unknown and varying

flow speeds through the restrictor between the manifolds and slits. The SST k–ω model was chosen specifically for its superior performance in resolving the viscous sublayers compared to the k–ϵ model. The flow was modelled as steady state, as the interest lies in the mean flow properties. All "Continua" models selected for the fluid setup are presented in Table 3.4.

Table 3.4: Continua Setup for the Fluid Flow

Group Box	**Model**
Space	Three Dimensional
Material	Liquid
Flow	Segregated Flow
Equation of State	Constant Density
Time	Steady
Viscous Regime	Turbulent
Turbulence Model	Reynolds-Averaged Navier Stokes
Turbulence Closure Model	k-ω
k-ω Turbulence Models	SST (Menter) k-ω
Wall Distance	Wall Distance*
k-ω Wall Treatment	Low y+ Wall Treatment
Additional Models	Solution Interpolation

Following the initial setup of the fluid continua, several parameter modifications were required. The liquid density and dynamic viscosity were updated to the values listed in Table 3.5. The turbulence specification was also set to "k+ω" for both the "Inlets" and the entire continua in order to accommodate to the initial velocity field being zero. Additionally, the reference pressure was set to two bar, representing an overpressure in machine of one bar above atmospheric pressure. The atmospheric pressure is assumed to be one bar as well.

Table 3.5: Properties of the VG2 Oil

Property	Symbol	Value	Unit
Density	ρ	790	$\frac{kg}{m^3}$
Dynamic Viscosity	μ	0.001738	$Pa \cdot s$

Reports were created, from which monitors and plots were generated. These reports included the force due to pressure and shear in the z-direction, the centre of the loads in the x- and y-direction, the mass flows, and the torque around the z-axis. The force, torque, and centre of load were evaluated for the rotor surfaces, while mass flow was monitored across the inlets, outlets, and the IF surfaces. This was done to ensure that the key variables and flow properties had converged, rather than relying only on the residuals. Note that the centre of load, force and torque reports were found at a late stage and were not implemented for all models.

3.5 Post-Processing

To visualize the results, two different methods were used. The scalar scenes in STAR-CCM+ was used to display some of the variables like pressure, y^+, tangential velocities etc.

Some data were extracted and exported as .csv files and imported into MATLAB for further processing. The first dataset included the cell index, cell centroid coordinates, cell area, wall shear components, and pressure. All of this data were extracted from the rotor surface. The second dataset comprised cell coordinates and index, cell volume, and absolute pressure, extracted from all cells in the domain. A third dataset included the residual and key variable plot data obtained from the simulation.

The viscous friction acting on the rotating disc results in power consumption. This power can be calculated using Eq. 2.5. However, the available simulation output provides shear stress rather than force or torque. To convert shear stress into force, Eq. 2.4 was used. This equation assumes that the cells are sufficiently small for the shear stress to be considered constant across the cell area. This assumption was applied to the extracted cell data. Accordingly, the force vector for each cell was computed by multiplying the wall shear components by the corresponding cell area, as described by Eq. 2.4.

To determine power from the force, the corresponding velocity vector is required. As the velocity field was not directly available, the known angular velocity was used instead. Power can also be calculated using angular speed if torque is known. Since the force vectors for each cell had already been determined and the cell coordinate was known, they were used to compute the torque vector for each cell by applying Eq. 2.1. These calculations were performed for all cells to obtain both the individual force and torque vectors.

The total torque vector resulting from viscous friction was then obtained by summing the torque contributions from all cells, as defined by Eq. 2.2. This total torque corresponds to a 120^o section of the full 360-degree disc. Given the rotational symmetry of the geometry, it was assumed due to the rotational symmetry that each of the remaining two 120^o sections experiences an identical torque. Additionally, the disc has two symmetric sides, and the same torque distribution was assumed for the opposite side as well due to the symmetry. An exception was made for the rotors with tilted rotors since the total power consumed by one rotor disc would be one thin gap side consumption plus one thick gap side consumption. Therefore, the total torque vector for the entire disc was calculated as:

$$\mathbf{M}_{tot} = 2 \cdot 3 \cdot \mathbf{M}_{120} \tag{3.1}$$

Once the total torque vector had been determined, the power consumed by viscous friction was calculated by multiplying each component of the torque vector by the corresponding component of angular velocity. Since rotation occurs only around the z-axis, only the M_z component of the torque vector was relevant. The system

includes seven rotor discs in total, so the total power loss due to viscous friction was obtained by multiplying the power consumed by a single disc by the number of discs. A code flow chart illustrating this calculation is provided in Figure 3.11.

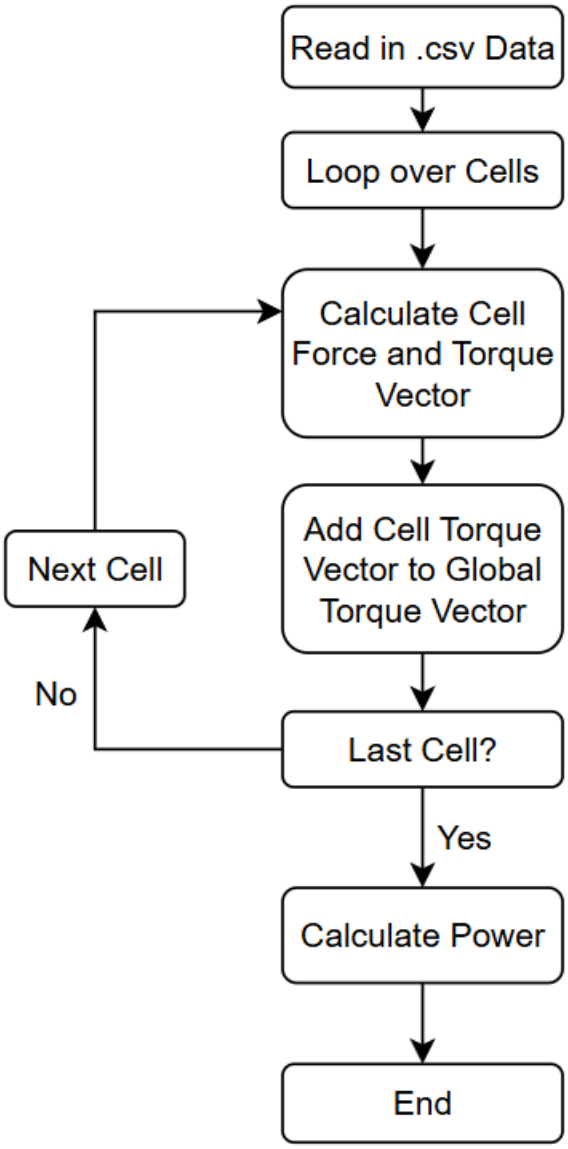

Figure 3.11: Code Flow Chart for Power Calculations

Another aspect of interest was the variation in torque around the inner radius when the rotor disc deflects. The setup represented the case of maximum allowable disc deflection, specified as 0.02 mm by Hagnesia. Due to the lack of material property data for the rotor disc, a simplified tilt was applied to the geometry to achieve the specified deflection at the outer edge as shown in Figure 3.4. These geometries got the same data extracted as mentioned at the start of Section 3.5. The same calculations was made for the power consumptions for these geometries.

The rotor surface was divided into even angular sections spanning from one edge to the other, as illustrated in Figure 3.12. A loop was then performed over all surface

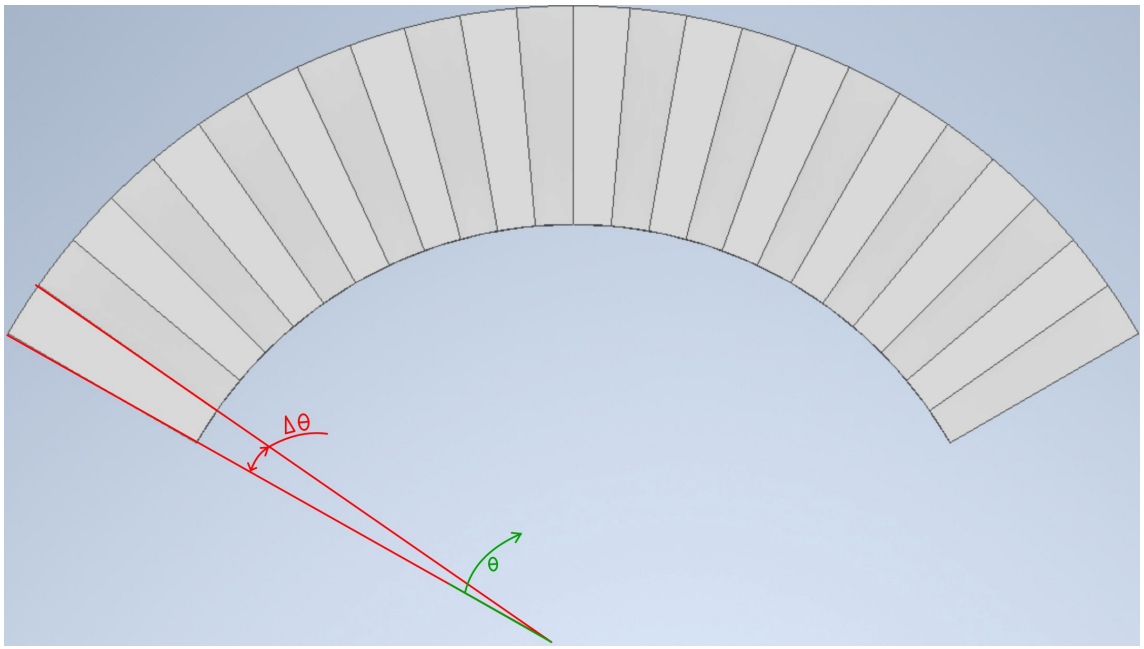

Figure 3.12: Clarification of Angular Sectioning and Angular Coordinate System Used

cells. Although each cell contains values that may vary across its area, the data were assumed to be constant within each cell due to their small size. Within the loop, each cell's coordinates were converted from Cartesian to polar. The force acting on each cell, due to pressure, was then computed using Eq. 3.2:

$$F = P \cdot dA \tag{3.2}$$

Since the force results from pressure, it acts perpendicularly to the surface. This allowed for calculation of the torque about the inner radius using Eq. 3.3 where alpha is the tilt angle given to the rotor:

$$M_{cell} = F_{cell} \frac{(r_{cell} - r_{inner})}{cos(\alpha)} \tag{3.3}$$

Each cell's torque was assigned to the appropriate angular section and the total torque for each section was accumulated from each cell's contribution. These section wise torque values were then visualized as a contour plot, where each angular segment was colour coded according to its total torque around the inner radius. Calculations were carried out for both disc sides, one for the thicker and one for the thinner gap. For each angular section, the torque from the side with the wider gap was subtracted from the torque on the thinner gap side, yielding the torque resisting the disc's tilting for each angular section. This torque is trying to bend the disc back in to the equilibrated state. A function was constructed as well to represent the imbalance torque between disc sides as a function of angle. This function was computed by dividing each section's total torque imbalance by the angular width of the section. A flow chart of code for the torque calculations can be seen in Figure 3.13. The MATLAB codes used to perform both the power consumption and torque

calculations are provided in Appendix A.1.

The residual and key variable data were directly imported into MATLAB and assigned to variables for plotting. The absolute pressure data were analysed to determine the minimum pressure values in the domain, which were then compared to the vapour pressure of VG2 to assess the risk of cavitation. The pressure distribution on the rotor surface was also processed in MATLAB to determine the maximum pressure difference caused by changes in geometry. A pressure concentration was observed near the "Slit" and "Manifold" connection, indicating that the absolute maximum pressure may not provide a reliable measure of geometric effects. To address this, the maximum pressure was extracted excluding the values from cells below the inlet from the "Manifold" to the "Slits". This was done by looping through each cell, converting the coordinates to polar form, and filtering out those whose radial and angular positions matched the pressure concentration regions.

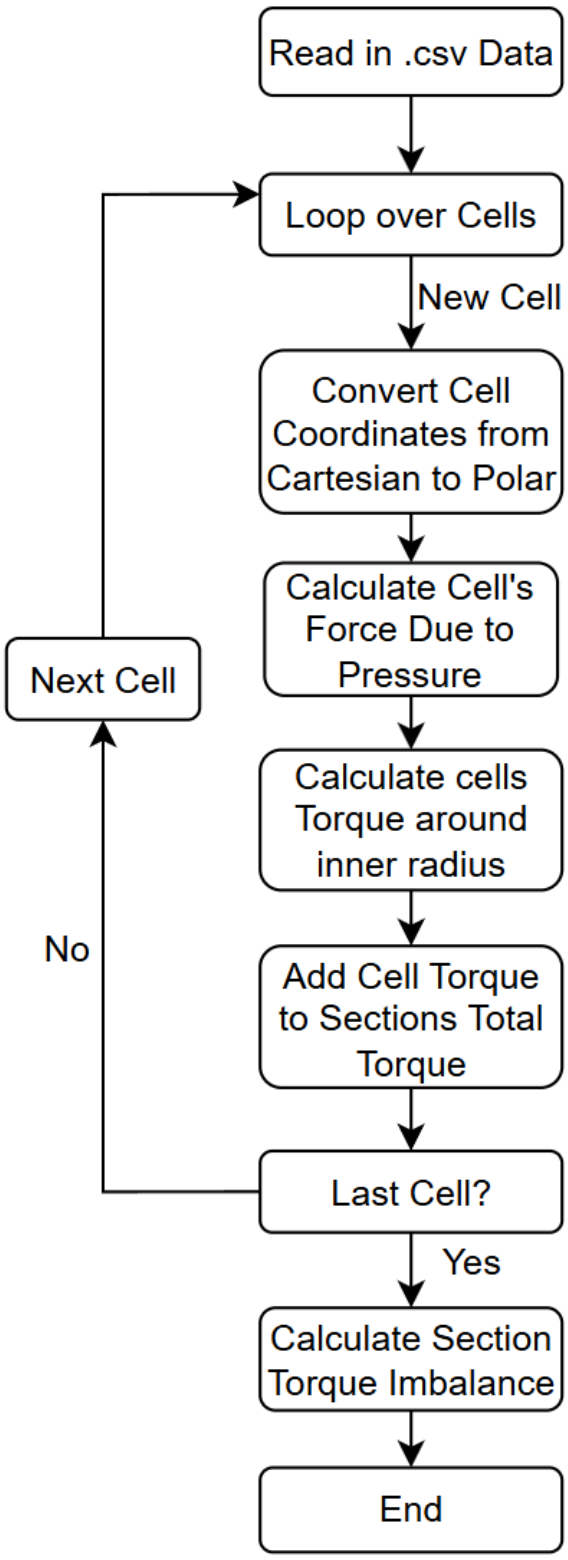

Figure 3.13: Code Flow Chart for Torque as a Function of the Angle

4

Results

This chapter presents the results obtained from the simulations. This includes the mesh for the different domains, pressure distributions, potential risk of cavitation, power consumption due to viscous friction, and the fluid's response to rotor tilt.

4.1 Mesh Result

In Figure 4.1 a view of the mesh over the entire domain can be seen, where the colour indicates the cell volume at the surface. The view in this figure is of the stator surfaces and the rotor surface can be seen in Figure 4.2.

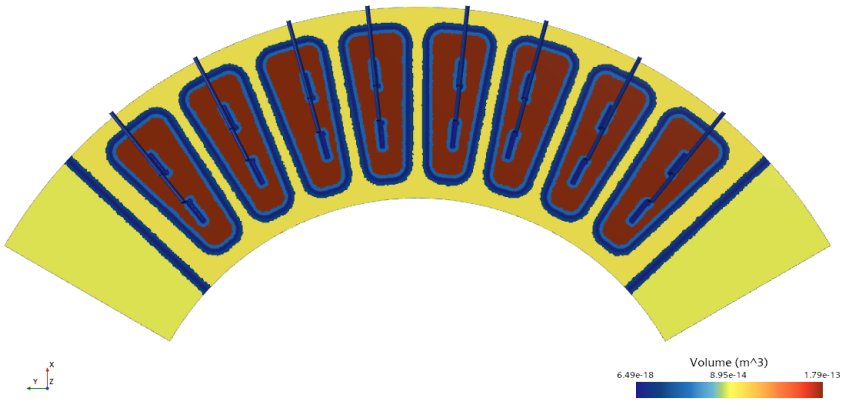

Figure 4.1: Cell Size as a Colour Shaded Plot Looking at the Stator Surfaces

Figure 4.2: Cell Size as a Colour Shaded Plot Looking at the Rotor Surfaces

In Figure 4.3, a meshed pocket is shown, where the mesh is illustrated using cell contours rather than colour shading. The mesh structure at the connection between the lands and the recess pockets is depicted in Figures 4.4 and 4.5. Figure 4.4 shows the corner region for the Basic (looks similar for Original as well), while Figure 4.5 displays the mesh for the geometry with five mm filleted pockets.

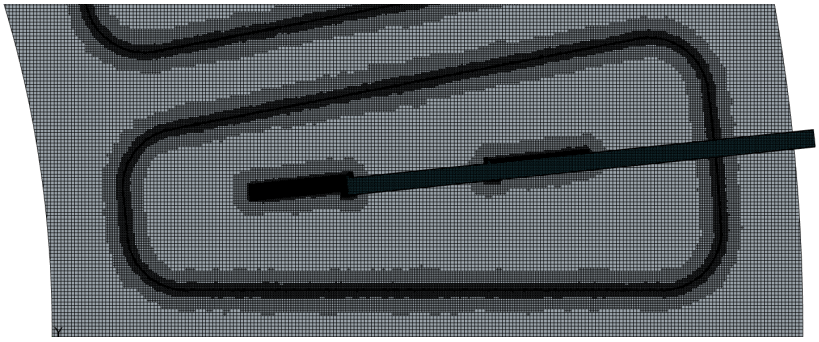

Figure 4.3: Mesh Over a Pocket With Cell Contours

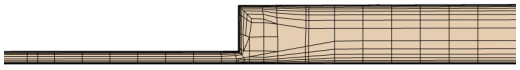

Figure 4.4: Mesh in Connection Land Gap/Recess Pocket for Full Depth Sharp Cornered Pockets

Figure 4.5: Mesh in Connection Land Gap/Recess Pocket for 5 mm Fillet Geometry

Throughout the domain, the first prism layer height was maintained below two μm. However, some local issues were observed at the "Slits" surface, primarily due to the slit shape. Similar issues also occurred at the interface between the "Slits" and "Manifolds". Although Figure 4.6 suggests a uniform first prism layer thickness across the entire domain, a closer view of the "Slits", as shown in Figure 4.7, reveals a significantly thicker first layer in some areas.

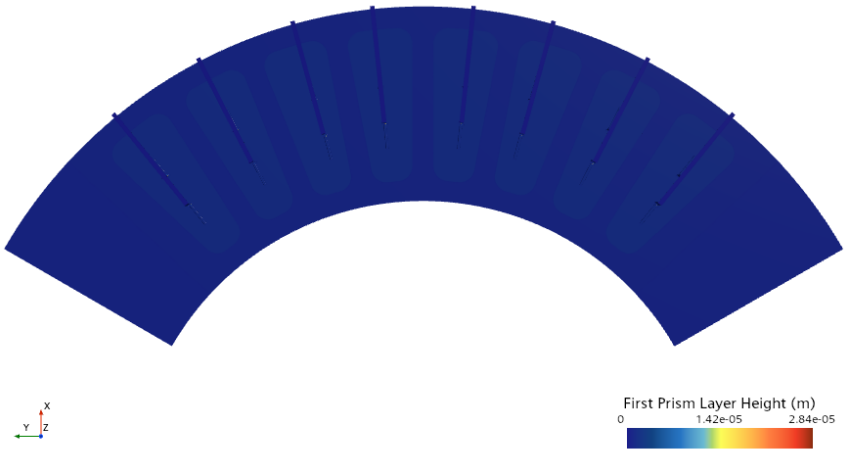

Figure 4.6: First Prism Layer Thickness Over the Domain

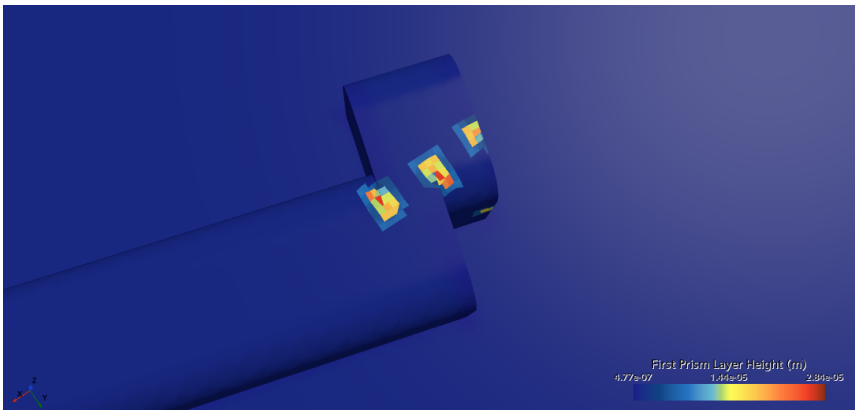

Figure 4.7: First Prism Layer Thickness on the "Slits" Near the "Manifold"

The total number of cells for each geometry can be seen in Table 4.1.

Table 4.1: Number of Cells for Each Geometry

Geometry	Number of Million Cells
Original	21.44
Thin Pockets	24.60
Fillet 2 mm	30.88
Fillet 5mm	29.81
Basic	20.67
Original Thin	21.02
Original Thick	22.10
Basic Thin	20.39
Basic Thick	21.26

4.2 Simulation Result

This section presents the results obtained from the simulations. It includes visualizations of pressure distributions, total power consumption, and the effects of rotor tilt on pressure behaviour and losses. The plots for the flow properties do not begin at iteration zero. This is done in order to better highlight the trends and changes in the data.

4.2.1 Basic Geometry

First up is too verify that the results are correct. To do this several different flow properties was monitored to make sure those properties converges. The residuals for the x, y, and z momentum together with the continuity, turbulent kinetic energy and specific dissipation rate residuals can be seen in Figure 4.8.

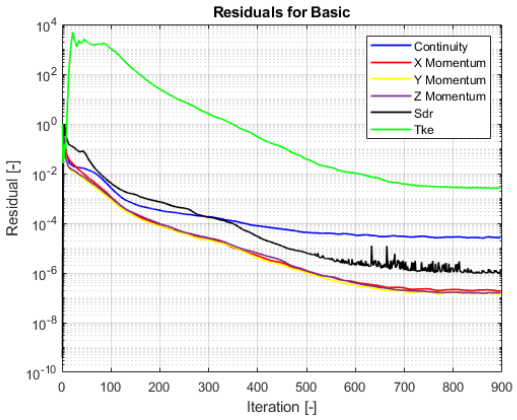

Figure 4.8: Residuals for Basic Geometry

Mass flows across the IF surfaces, inlet, and outlets, along with the total net mass flow, are presented in Figure 4.9. Figures 4.10 through 4.12 display the force in the z-direction due to pressure and shear, the torque about the z-axis from both pressure and shear, and the centre of load in the x- and y-direction on the rotor.

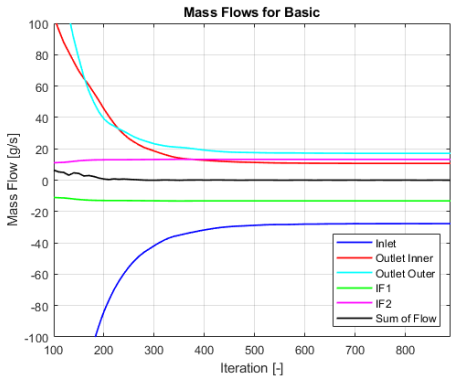

Figure 4.9: Mass Flows Over Boundaries for the Basic Geometry

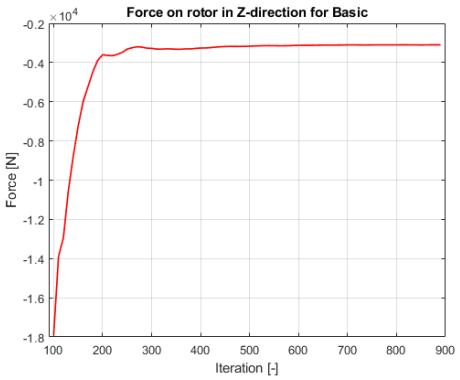

Figure 4.10: Force on the Rotor Surface for the Basic Geometry

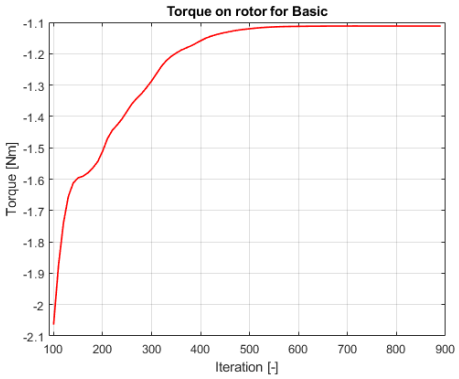

Figure 4.11: Torque for the Rotor Surface for Basic Geometry

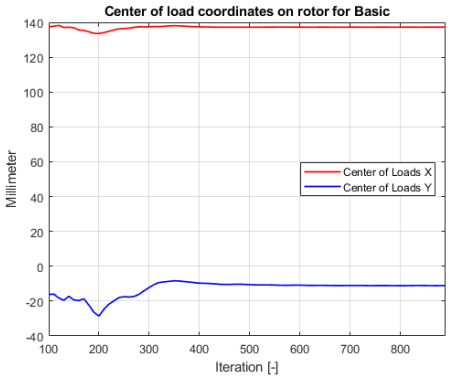

Figure 4.12: Centre of Loads for the Basic Geometry

From these plots, it is clear that all monitored properties have converged towards a final value. The mass flow plots confirm that no mass accumulation occurs over time and the mass flow over the interfaces is the same, all of which aligns with expectations. Also looking at the "Outlet Outer" it can be seen that the mass flow is larger there which also is as expected due to centrifugal forces pushing the fluid outwards and that the area of that outlet is larger. A plot of tangential velocity through a section of the geometry is shown in Figure 4.13 with a magnification of the fluid gap over the lands.

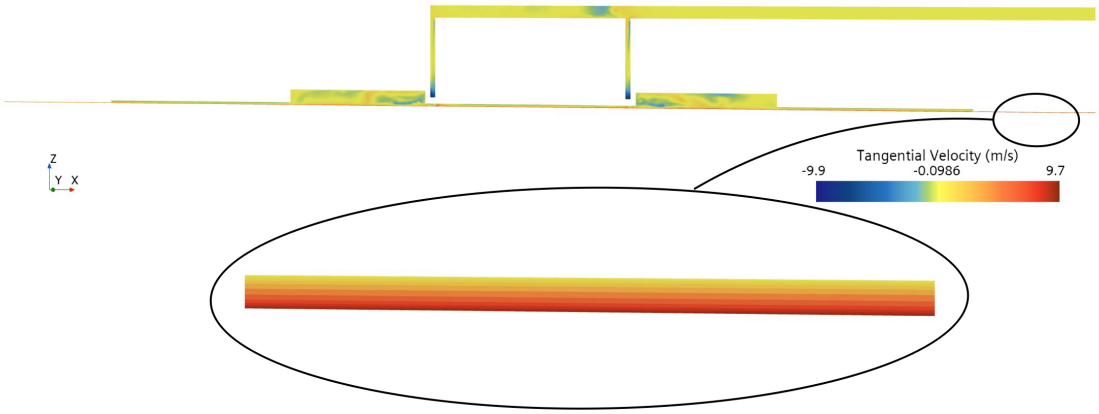

Figure 4.13: Tangential Velocity Through a Section with a Magnification for the Fluid Gap Between the Lands

As expected, the fluid velocity approaches the rotor velocity near the rotor surface and goes toward zero at stationary walls, confirming physically realistic boundary behaviour. Additional evidence of solution accuracy is provided by the pressure distribution across the domain, shown in Figure 4.14. As predicted by bearing theory, the highest pressure occurs at the pump supply in the "Manifold", followed by a drop when entering the recess pockets, and a further drop across the lands, reaching ambient pressure near the outlets. Furthermore, Figure 4.15 shows that the pressure within the recess pockets increases in the direction of rotation (counter-clockwise), which is also consistent with theoretical expectations.

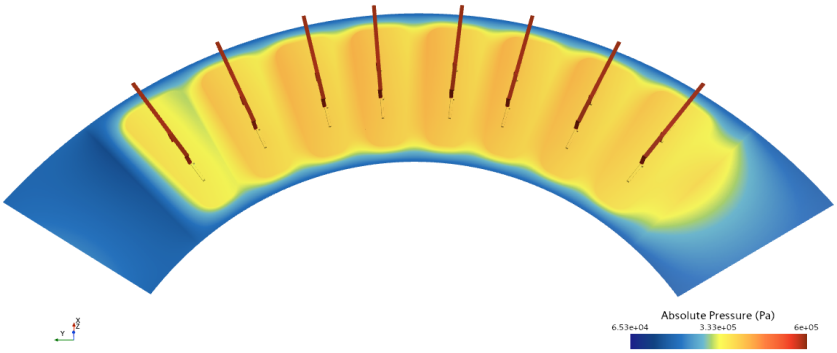

Figure 4.14: Absolute Pressure Distribution Over the Entire Domain

The results of the absolute pressure distribution are presented in Figure 4.15. The maximum absolute pressure on the rotor is 456.1 kPa, and the minimum is 149.4 kPa. Some pressure concentrations below the slits were observed. Without these concentrations the maximum pressure was equal to 425.4 kPa and is the maximum pressure due to the geometric shape of the pockets. The absolute pressure field is obtained by adding the ambient pressure of two bar (200 kPa) to the working pressure field from the simulation.

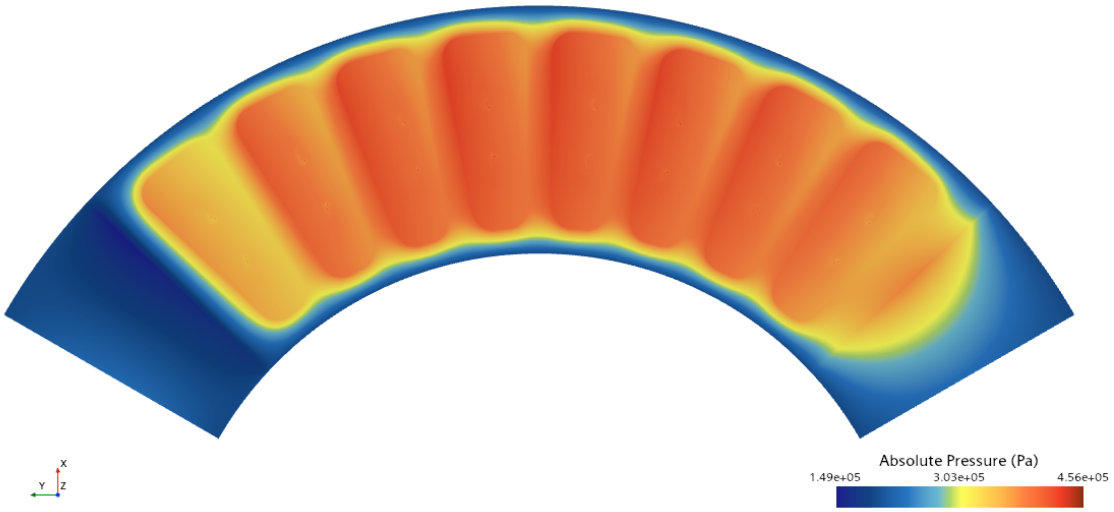

Figure 4.15: Absolute Pressure Distribution on the Rotor Surface for the Basic Geometry

The torque around the z-axis acting on the rotor surface in the simulation due to wall shear stress is calculated to be -1.1118 Nm. The value for one entire disc, composed of six of the simulated sections gives a torque of -6.6707 Nm per rotor disc. As a result, the power consumption due to viscous friction for a single disc is 349.3 W which in turn means that for a machine of seven discs the total viscous power loss is 2445 W.

The lowest absolute pressure in the entire domain was found to be 65.26 kPa, which remains well above the vapour pressure (134 Pa) of the fluid. This indicates that

cavitation is unlikely to occur under the operating conditions which the simulation is made for.

It was also observed that the y^+ values exceed the recommended minimum threshold of three in certain regions. These areas coincide with the regions where the first prism layer is noticeably thicker, particularly in the "Slits" adjacent to the "Manifold", as shown in Figure 4.16. This observation aligns with Figure 4.7, confirming that the elevated y^+ values occur where larger prism layer cells are present.

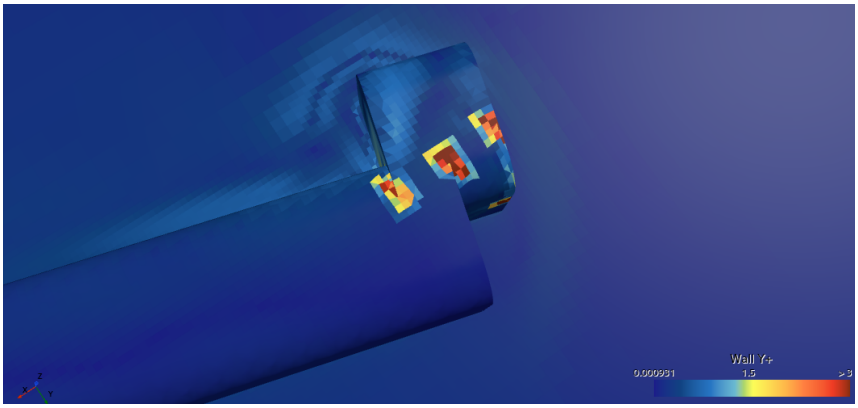

Figure 4.16: Plot of y^+ at "Manifold" and "Slits" Connection

According to turbulence modelling theory and the chosen wall treatment approach, boundary conditions may not be applied correctly in regions where y^+ exceeds the target range. This can introduce numerical inaccuracies in those specific zones. However, these regions are located far from the rotor surfaces, where the primary quantities of interest (pressure distribution and power consumption) are evaluated. Therefore, while the elevated y^+ values may introduce some localized errors, their influence on the overall results is considered acceptable.

4.2.2 Geometries without Tilted Rotors

The residuals for each of the simulations, along with mass flows, torques, forces, and load locations, are provided in Appendix A.2, along with visualizations of the geometries in which the fluid film thickness varies. All simulations, including those for the Basic geometry, demonstrated convergence in mass flow rates, forces, torques, and centre of load positions. Additionally, the residuals converged towards final values as well.

The pressure distributions and velocity profiles for these cases exhibit trends similar to those observed in the Basic geometry. The pressure distribution across both the rotor surface and the entire domain follows similar shapes and patterns. The pressure throughout the entire domain varies between the manifolds, pockets, and lands in a manner that is to be expected from the bearing theory.

On the rotor surface, the centrally located pockets display the highest pressures, while the edge pockets exhibit comparatively lower pressures. Within each pocket,

the pressure increases in the rotors direction of rotation, which is consistent with theoretical predictions. The radial location of the maximum pressure though is closer to the middle of the radial span in domain rather than further towards the outer edge as for the Basic. Additionally the maximum and minimum absolute pressure values differ between the geometries as well. These values for each geometry on the rotor surface are summarized in Table 4.2.

Table 4.2: Minimum and Maximum Absolute Pressure the Rotor Surface for the Geometries

Geometry	$\mathbf{P}_{abs,min}$ [kPa]	$\mathbf{P}_{abs,max}$ [kPa]
Original	145.7	465.6
Shallow	151.4	480.8
2 mm Fillet	145.9	466.1
5 mm Fillet	146.0	466.1

An additional issue was identified involving pressure concentrations near the connection between the "Slits" and "Manifold". These regions contain the maximum pressure values on the rotor surface. However, since the focus is on understanding how pocket geometry influences pressure, a filtered maximum pressure was calculated by excluding the pressure concentration areas below the "Slits". These adjusted values are presented in Table 4.3.

Table 4.3: Minimum and Maximum Absolute Pressure on the Rotor Due to Geometric Difference of Pockets

Geometry	$\mathbf{P}_{abs,min}$ [kPa]	$\mathbf{P}_{abs,max}$ [kPa]
Original	145.7	434.4
Shallow	151.4	456.1
2 mm Fillet	145.9	435.2
5 mm Fillet	146.0	437.2

Each pocket profile subjected the rotor surface to different levels of torque as a result from wall shear stresses. The torque experienced by the rotor surface in each simulation is listed in Table 4.4 together with the total torque for one complete disc, and the corresponding power consumption due to friction, both per disc and for an entire machine.

Table 4.4: Torque and Power Result for Equilibrium Geometries

Geometry	$\mathbf{M}_{120}$ [Nm]	$\mathbf{M}_{disc}$ [Nm]	$\mathbf{P}_{disc}$ [W]	$\mathbf{P}_{tot}$ [W]
Original	-1.1343	-6.8060	356.4	2 494.5
Shallow	-1.1338	-6.8031	356.2	2 493.5
2 mm Fillet	-1.1342	-6.8053	356.3	2 494.3
5 mm Fillet	-1.1344	-6.8064	356.4	2 494.7

Another key result is the lowest absolute pressure observed in the domain for each geometry. These minimum values are presented in Table 4.5. All geometries demon-

strated minimum pressures well above the vapour pressure of 134 Pa, indicating that cavitation is unlikely to occur under the simulated conditions

Table 4.5: Lowest Absolute Pressures in the Entire Domain

Geometry	$\mathbf{P}_{abs,min}$ [kPa]
Original	90.92
Shallow	32.89
2 mm Fillet	65.93
5 mm Fillet	85.34

4.2.3 Geometries with a tilted rotor

As described in Section 4.2.2, the residuals, along with plots of mass flow, torque, force, and centre of load, are presented in Appendix A.2. These plots show that all monitored properties have converged satisfactorily. The pressure distribution over the manifolds, pockets, and lands follows the expected trends described by bearing theory just as the results observed for the Basic geometry. Additionally, it can be seen that in the thinner gap configuration, the "Outer Outlet" mass flow decreases, as anticipated, due to the increased resistance to flow through the narrower outlet opening. In contrast, the thicker gap configuration exhibits an increase in mass flow through the "Outer Outlet", as the reduced resistance allows for easier flow. This behaviour is observed consistently in both geometries modelled with thicker and thinner gaps.

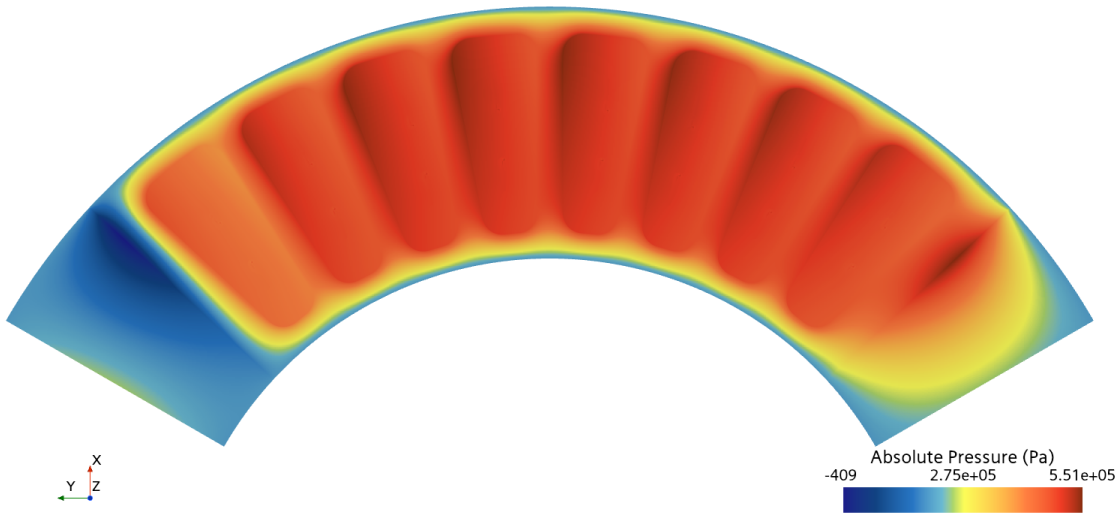

Figure 4.17: Absolute Pressure Distribution on the Rotor for Basic with a Thinner Gap

The pressure distribution in the tilted configurations follows a similar pattern to that observed in the undeformed geometries, with higher pressures in the central pockets with elevated pressures on the side of the pocket facing the direction of

rotation. Figure 4.17 and 4.18 shows the pressure distribution for the Basic thinner and thicker gap geometries. However, differences are observed in both the magnitude and the radial distribution of pressure. For the thinner gap side of the disc, pocket pressures have increased significantly compared to the equilibrium case described in Section 4.2.1 and 4.2.2. For the thinner gap geometries the pressure also increases with increasing radial coordinate. However, for the Original geometry this increase is significantly larger than for the Basic geometry. The thicker gap side on the other hand shows lower pressure magnitudes. The change in pressure in the radial coordinate direction for the thicker gap geometries is different between the Basic geometry and the original geometry. The Basic geometry does not vary significantly in the radial direction while there is a significant decrease in pressure with an increase in the radial coordinate for the Original geometry.

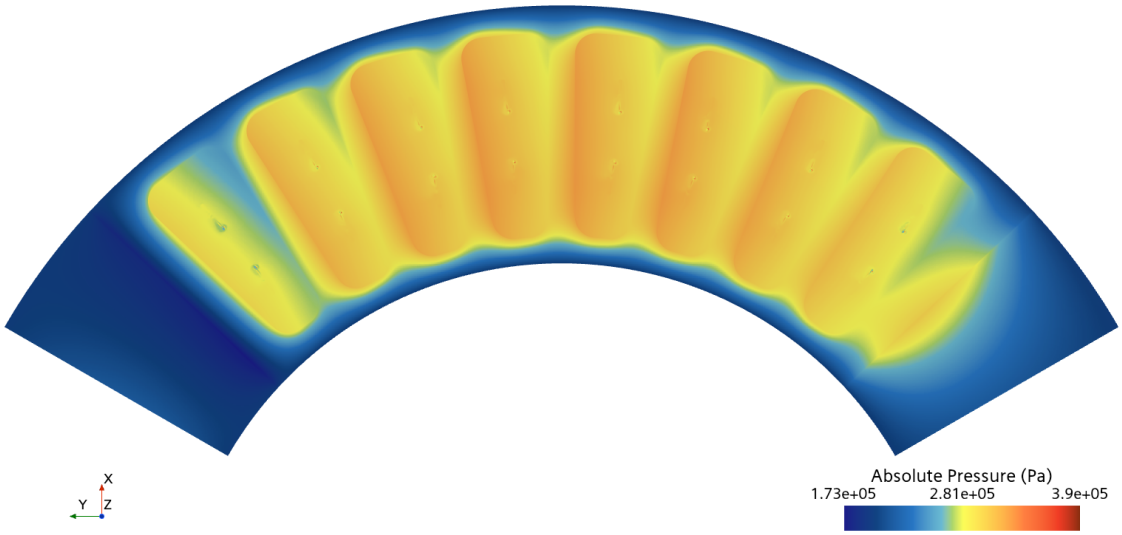

Figure 4.18: Absolute Pressure Distribution on the Rotor for Basic with a Thicker Gap

An approximate pressure at the inner and outer pocket radius for the left side of fifth pocket from the left in Figure 4.17 can be seen below in Table 4.6 as well to give an indication of how the pressure varies over a pocket.

Table 4.6: Pressure at Inner and Outer Radius of the Pocket Region

Model	$\mathbf{P}_{abs,inner}$ [kPa]	$\mathbf{P}_{abs,outer}$ [kPa]
Basic Thin	490	551
Basic Thick	310	330
Original Thin	450	590
Original Thick	360	300

The maximum and minimum absolute pressures for the Basic geometries can be seen in the previously mentioned pressure distribution figures. The Original geometries pressure distributions on the rotor differs in maximum and minimum values from

the Basic and are listed in Table 4.7. The torque values acting on each rotor section, along with the total torque and power consumption for a deformed disc, both the Basic and Original„ are presented in Table 4.9.

Table 4.7: Absolute Pressure on the Rotor Surface for the Original Geometry with a Tilted Rotor

Geometry	$\mathbf{P}_{abs,min}$ [kPa]	$\mathbf{P}_{abs,max}$ [kPa]
OP. Thin	-0.4	551.3
OP. Thick	173.0	389.9
Original Thin	1.0	590.1
Original Thick	175.9	421.4

In the thinner gap geometries, pocket pressures reach values so high that the pressure concentrations at the "Slits" and "Manifold" connection no longer are the maximum pressures within the domain. This is not the case for the thicker gap configurations, where the slit region still contains the highest pressures. The maximum pressures excluding the concentration region are presented in Table 4.8.

Table 4.8: Maximum Absolute Pressure on the Rotor Surface for the Thicker Gap Geometries Excluding the Concentrations

Geometry	$\mathbf{P}_{abs,max}$ [kPa]
OP Thick	330.2
Original Thick	365.7

Table 4.9: Torque and Power Results for Geometries with Tilted Rotor Discs

Model	$\mathbf{M}_{120}$ [Nm]	$\mathbf{M}_{disc}$ [Nm]	$\mathbf{P}_{disc}$ [W]
Basic Thin	-1.5062	-7.2578	380
Basic Thick	-0.9131		
Original Thin	-1.5486	-7.4206	388.5
Original Thick	-0.9250		

The imposed deformation introduces a pressure imbalance between the thin and thick gap sides of the disc, resulting in a torque around the inner radius. This torque is visualized through colour contour plots, with each angular segment shaded according to the torque it is subject to. The result for the Basic geometry is shown in Figure 4.19, while the result for the Original geometry is presented in Figure 4.20. The inner radius is indicated by a dashed black line.

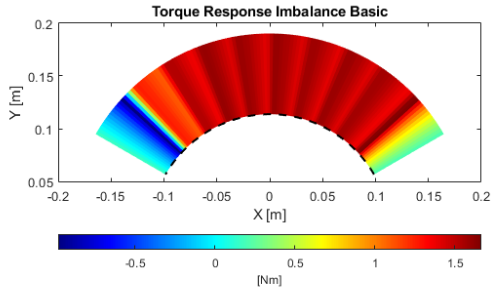

Figure 4.19: Torque Around Inner Radius Counteracting Pressure Difference for Basic Geometry

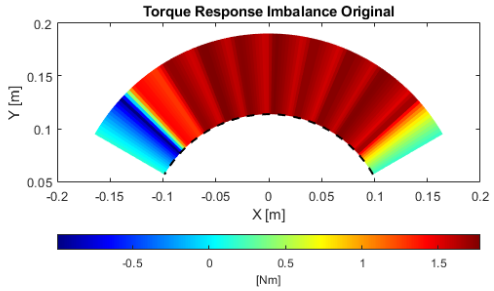

Figure 4.20: Torque Around Inner Radius Counteracting Pressure Difference for Original Geometry

The torque distribution can be expressed as a function of the angular coordinate, which follows the angular coordinates displayed in Figure 3.12. The resulting torque functions are plotted in Figures 4.21 and 4.22 for the Basic and Original geometries respectively.

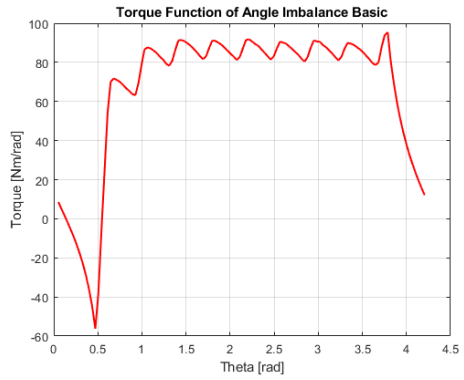

Figure 4.21: Torque Around Inner Radius as a Function of the Angle for Basic Geometry

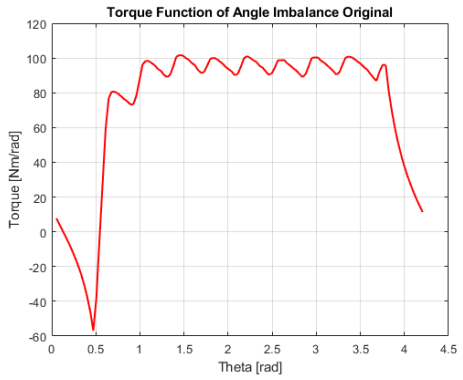

Figure 4.22: Torque Around Inner Radius as a Function of the Angle for Original Geometry

Lowest absolute pressure across the tilted rotor domains was extracted and presented in Table 4.10. It can be observed that an unphysical absolute pressure value, lower than zero, occurred. This appeared in all four of the domains. For the thicker gap geometries, the absolute pressure was significantly lower compared to the thinner gap configurations.

Table 4.10: Lowest Absolute Pressures in Entire Domain for Tilted Rotor Geometries

Geometry	$\mathbf{P}_{abs,min}$ [kPa]
Original Thick	-65.86
Original Thin	-3.18
Basic Thick	-128.79
Basic Thin	-3.83

A difference between the thinner and thicker gap geometries regarding the minimum absolute pressure is that there are a lot of cells in the same region experiencing the low pressures for the thinner gap geometries. The thicker gap geometries on the other hand has only a few cells experiencing the negative pressure and those cells are surrounded by positive pressure cells. The cells are located in the "Slits" and "Manifold" connection area. In Figure 4.23 a plot of a section cutting some of the negative pressured cells for the Basic geometry with a thicker gap.

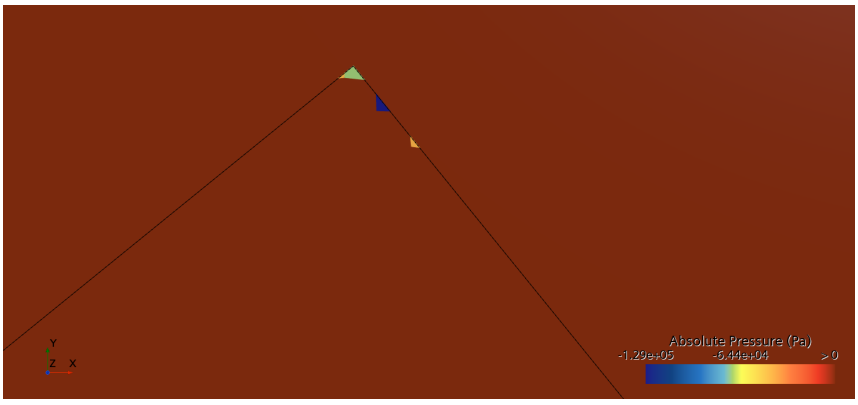

Figure 4.23: Cells with Negative Pressure with Neighbouring Positive Pressured Cells

4.3 Torque and force

The torque around the z-axis and the force in the z-direction were calculated using both MATLAB and STAR-CCM+ for a subset of the geometries, while others were evaluated using the MATLAB code only. The results from both calculation methods are presented in Table 4.11.

Table 4.11: Torque and Force Value Comparison Between MATLAB and STAR-CCM+

Geometry	$\mathbf{M}_{MATLAB}$ [Nm]	$\mathbf{M}_{STAR}$ [Nm]	$\mathbf{F}_{MATLAB}$ [N]	$\mathbf{F}_{STAR}$ [N]
Original	-1.1343	-1.1343	3098	3097
Thin Pockets	-1.1338	-1.1338	3146	3146
Fillet 2 mm	-1.1342	-1.1342	3097	3097
Fillet 5mm	-1.344	-1.344	3103	3102
Basic	-1.1118	-1.1118	3099	3098
Original Thin	-1.5486	-1.5486	5002	5002
Original Thick	-0.9250	-	1817	-
Basic Thin	-1.5062	-	4865	-
Basic Thick	-0.9131	-0.9131	1663	1663

5
Discussion

One thing that may have affected the results is the MATLAB code calculation of the torque and force. The function of generating reports of these variables was found late meaning that not all of the simulation had time to be simulated again. Table 4.11 can be found in Section 4.3 and it presents the values of the torque and force from both MATLAB and STAR-CCM+.

The table shows that the torques differ by nothing down to the fourth decimal, deeming the MATLAB calculations a sufficient method with adequate assumptions. The forces differ a bit more, with the largest difference being 0.032%. This difference is not significant, meaning that the MATLAB calculations can also be deemed sufficient with adequate assumptions for the force calculations. Also, looking at the convergence plots, it can be seen that all of the plots seem to reach convergence for both force and torque before iteration 700, and all simulations ran for at least 800 iterations. Comparing the force and torque plots to the residual plots, it can also be seen that for all the simulated geometries, the force and torque have converged once all of the residuals have flattened out. All simulations were run until that happened, also supporting convergence for the torque and force in the simulations not using the torque and force diagrams.

An additional issue in MATLAB is the torque response calculations for the tilted rotor. The issue is in the method that introduces a potential source of error: some cells may partially contribute to the wrong section. This occurs because the cell centre coordinate is used to assign sections, and a centre point located in one section does not guarantee that the entire cell lies within that region. However, this issue is mitigated if the angular section width is sufficiently large relative to the cell size. This is due to small cells and relative large angular sections which means that small cell areas crosses the boundaries compared to the total area of the angular section. An additional issue in MATLAB is the torque response calculations for the tilted rotor. The issue lies in the method, which introduces a potential source of error which is some cells may partially contribute to the wrong section. This occurs because the cell centre coordinate is used to assign sections, and a centre point located in one section does not guarantee that the entire cell lies within that region. However, this issue is mitigated if the angular section width is sufficiently large relative to the cell size. This is due to the small cells and relatively large angular sections, which means that only small cell areas cross the boundaries compared to the total area of the angular section.

It could be interesting to investigate the possibility of deeper recess pockets. If it

follows the same trend as seen when comparing the pressure of the Original and Shallow geometry, it would mean that a lower pocket pressure in the equilibrated state could be acquired. A lower pressure in the equilibrated state means, according to hydrostatic bearing theory, a potentially larger pressure increase in the pocket when the fluid film thickness is decreased. A larger pressure increase means that it might make the geometry even more rigid, meaning a greater ability to withstand higher magnetic forces. It might also make it stiff enough not to require changes to the geometry in areas where there is a risk of cavitation. This might be the case because a more rigid rotor means less deflection, meaning that a 0.02 mm deflection of the outer edge might not occur if the rotor is more rigid. Since the rotor disc, in a perfect installation, should be in the equilibrium state, the lower pressure in the pockets should not be an issue. The possible increase in torque trying to push the rotor back to equilibrium when deflected is of greater interest than a high pressures in the equilibrium state.

Another challenge to address further is the absolute pressure for the deflected rotor. For both of the geometries with a thicker gap, the lowest absolute pressures were very low, below -50 kPa. The negatively valued cells, however, were single cells with larger positive pressures beside them, and the locations of the cells were on the "Slits", adjacent to the "Manifold", meaning the larger y^+ values might be what causes this. The number of cells experiencing these low pressures was only about ten out of over 20 million cells. This, in addition to the fact that the cells adjacent to the negatively pressured cells have positive pressure values, indicates that something is not correct.

The thinner gap geometries, on the other hand, have a larger region with a greater number of cells exhibiting negative absolute pressure, and they are also located in the same region, not like the thicker gap ones, which were scattered over different slits. This suggests that there is likely an issue with cavitation here, and that modelling the flow as single-phase flow could be a reason for the unphysical negative absolute pressure values. Further studies should be conducted to determine whether the geometry in the negative pressure region could be modified to avoid this issue, or if it is necessary to increase the ambient pressure in the machine. Increasing the pressure in the machine could lead to leakage, and it would be preferable to avoid increasing the ambient pressure.

In general looking over the different geometries it can be seen that the power consumption between the equilibrium state geometries are somewhere in between the range of 2445 to 2495 W which means that the highest consuming geometry consumes 2.04 % more energy than the lowest consuming geometry. Lowest consuming geometry is the Basic while the other remaining four geometries only varies with less than two watts between each other. Putting this as a percent of the expected power delivery of the machine means a efficiency loss of 0.537% for the Basic while the others have a 0.545% loss.

Over the part of the geometry where the pockets are located it can clearly be seen that there is a pressure increase compared to outside the pocketed area. It shows

also how the pressure varies from the left to the right over the pocket. In the Figures 4.21 and 4.22 this can clearly be seen how the torque due to the pressure differs by almost 10 Nm per Rad from left to right over a pocket. Torque difference over the pocket for the Basic geometry corresponds to a 12.5 % increase between the sides. It also differs 10 Nm per Rad between the Original and Basic geometry with a higher torque for the Original geometry. The Original geometry is therefore more rigid and can withstand the magnetic forces better than the Basic geometry. The issue here is the power consumption where the power consumed when the rotor disc is deflected. If a disc is deflected the power consumption increases by 8.7 % for the Basic geometry compared to the equilibrium state while it increases with 9.0 % for the Original geometry.

A comparative analysis then reveals that geometries featuring a pocket layout derived from the Original design exhibit an increase in power consumption of approximately 2.04% compared to the Basic geometry, which only shows a 0.011 percentage point reduction in efficiency. Additionally, the Original geometry demonstrates a superior torque response, about 12% higher, which is a more significant difference than that observed in power consumption. This enhanced torque response is crucial for maintaining surface separation, making the Original geometry the more favourable option overall. However, further simulations are required to identify which of the Original-based pocket geometries delivers the best performance in terms of torque response.

Looking at the torque as a function of the angle, see Figures 4.21 and 4.22 , it can be seen that there is a negative torque actually increasing the tilting of the rotor right before the pockets, looking from the left. This response is not desired for the rotor. Lower pressure in this region for the thinner side compared to the thicker sides is what causes this and it results in a torque that increases the deflection of the rotor in this area. It is also in this area where cavitation is a risk. A solution to this could be increasing the ambient pressure. Higher ambient pressure means a higher pressure in the machine, which increases the risk of leakage. Increasing the ambient pressure might solve the cavitation but to solve the torque issue it might be needed to investigate whether a geometry change could be employed to avoid it.

Since the y^+ values were a bit high, further mesh refinements would be needed to resolve that issue. It would also be interesting to see whether this could solve the issue with the negative absolute pressure for the thick domain, or if there might be a cavitation issue in those areas. The mesh had problems generating the prism layers in the areas where the large y^+ occurred, and more time would be needed to solve this. A possibility could also be to change the geometry to see if it would help with generating the prism layers.

Unrealistic deformation of the rotor is also something that needs to be mentioned. Due to the simplifications made to make the work feasible in the dedicated time period, a simple linear deformation was used. In reality, the rotor would not deform in this linear manner, which would change how the pressure is distributed. One solution to this problem could have been to perform a finite element method analysis

of the rotor with a displacement control on the outer edge and observe how it would actually deform. The issue with this is that it requires material parameters for the rotor, which are unknown. Another solution could be to conduct a fluid-structure interaction simulation, but for that, the issue regarding the material parameters still remains.

6
Conclusion

An evaluation of power consumption across the different geometries shows that the variation is negligible. The difference between the maximum and minimum power consumption geometries is less than 50 W, which corresponds to approximately 0.011% of the total power delivered of the generator. This indicates that geometric changes have an insignificant impact on power demand under these conditions but there is a difference between the geometries.

In the uniformly thick fluid film, i.e. when no rotor tilting occurs, no risk of cavitation was observed for any of the geometries. However, tilting of the rotor introduces regions of low pressure, which may pose a risk of cavitation.

In general, the pressure distribution across the different equilibrium geometries does not vary significantly. The only geometry that exhibited a notable pressure increase is the geometry with shallow pockets. The total force acting on the rotor due to pressure and shear was found to be approximately 3100 N for most configurations, while the geometry with thinner recess pockets showed a slightly elevated force of approximately 3145 N.

When examining the pressure between the two geometries tested with a tilted rotor, significant differences in the pressure distribution can be seen with a lot higher pressure in the pocket regions towards the outer radius. The Original geometry was subjected to higher pressures and this can also be seen when analysing the restoring torque, i.e. the torque acting to return a tilted rotor to its original position. A noticeable difference was observed between the Basic and Original geometries where the Original geometry generated a restoring torque around the inner radius that was approximately 12% higher over the regions where the pockets are located, making it a preferable design in terms of rotor stability under deflection. The Original geometry also had a bigger difference in pressure between the inner and outer radial coordinates in the pockets. Taking the results into consideration it can be concluded that the Original geometry's pocket layout is the better choice, but to know exactly which one to choose, simulations with a tilted rotor is needed for the remaining geometries as well.

For future studies, simulating a geometry with deeper recess pockets could offer insights into performance and structural response during rotor deflection. Implementing a multiphase flow model would also help determine whether cavitation actually occurs in the observed low pressure regions. If cavitation occurs that needs to be further investigated and solved so the cavitation can be avoided.

Bibliography

[1] N. Gadiyar, J. Van Verdeghem and E. L. Severson, "A review of axial flux permanent magnet machine technology," *IEEE Transactions on Industry Applications*, vol. 59, no. 4, pp. 3920–3933, 2023. DOI: 10.1109/TIA.2023.3258933.

[2] YASA, "YASA Limited", [Online]. Available: https://yasa.com/.

[3] Magnax, "Magnax - Yokeless Axial Flux Technology". [Online]. Available: https://www.magnax.com/.

[4] A. Hagnestål, Private Communication, May, 2025.

[5] A. Cavagnino, M. Lazzari, F. Profumo and A. Tenconi, "A comparison between the axial flux and the radial flux structures for pm synchronous motors," *IEEE Transactions on Industry Applications*, vol. 38, no. 6, pp. 1517–1524, 2002. DOI: 10.1109/TIA.2002.805572.

[6] F. Giulii Capponi, G. De Donato and F. Caricchi, "Recent advances in axial-flux permanent-magnet machine technology," *IEEE Transactions on Industry Applications*, vol. 48, no. 6, pp. 2190–2205, 2012. DOI: 10.1109/TIA.2012.2226854.

[7] S. Amin, S. Khan and S. S. Hussain Bukhari, "A comprehensive review on axial flux machines and its applications," in *2019 2nd International Conference on Computing, Mathematics and Engineering Technologies (iCoMET)*, 2019, pp. 1–7. DOI: 10.1109/ICOMET.2019.8673422.

[8] S. Kahourzade, A. Mahmoudi, H. W. Ping and M. N. Uddin, "A comprehensive review of axial-flux permanent-magnet machines," *Canadian Journal of Electrical and Computer Engineering*, vol. 37, no. 1, pp. 19–33, 2014. DOI: 10.1109/CJECE.2014.2309322.

[9] J. Colton, D. Patterson and J. Hudgins, "Design of a low-cost and efficient integrated starter-alternator," in *2008 4th IET Conference on Power Electronics, Machines and Drives*, 2008, pp. 357–361. DOI: 10.1049/cp:20080543.

[10] V. e. a. Schneider, "Electrical bearing damage, a problem in the nano- and macro-range," *Lubricants*, vol. 10, no. 5, May 2022. [Online]. Available: https://www.mdpi.com/2075-4442/10/8/194 (Accessed on: 19/5/2025).

[11] SKF, *Rullningslager*. SKF-concernern, 2019, ch. A.

[12] T. Someya, *Journal-Bearing Databook*. Springer Science Business Media, 1989, ch. 1.

[13] P.-Å. Jansson, R. Grahn and M. Enelund, *Mekanik: Statik och Dynamik*, 4th. Studentlitteratur, 2018, ch. 7, pp. 230–231.

[14] H. Versteeg and W. Malalasekera, *An Introduction to Computational Fluid Dynamics: The Finite Volume Method*. 2007, pp. 12–24.

[15] A. Poznyak, *Advanced Mathematical Tools for Control Engineers: Volume 1*. Elsevier, 2010, p. 332.
[16] M. Ekh, *Mechanics of solids and fluids -introduction to continuum mechanics*, 2022.
[17] F. M. White and R. Y. Chul, *Fluid Mechanics*. 2016, 211-212:308:407–408.
[18] L. Davidson, *Fluid mechanics, turbulent flow and turbulence modeling*, eBook, Division of Fluid Dynamics, Dept. of Mechanics and Maritime Sciences, Chalmers University of Technology, Gothenburg, 2022. [Online]. Available: `https://www.tfd.chalmers.se/~lada/postscript_files/solids-and-fluids_turbulent-flow_turbulence-modelling.pdf`.
[19] L. Davidson, "An introduction to turbulence models," Dept. of Thermo and Fluid Dynamics, Chalmers University of Technology, Gothenburg, Tech. Rep. 97/2, 1997. [Online]. Available: `https://www.tfd.chalmers.se/~lada/postscript_files/kompendium_turb.pdf`.
[20] J. Blazek, *Computational fluid dynamics principles and applications*. Butterworth-Heinemann, 2015, ch. 7.
[21] A. F. Molland and S. R. Turnock, *Marine Rudders, Hydrofoils and Control Surfaces*. Butterworth-Heinemann, 2021, ch. 6.8.
[22] Siemens Digital Industries Software, *Simcenter star-ccm+ documentation*, Hämtad: 2024-04-16, Siemens Digital Industries Software, 2020. [Online]. Available: `https://docs.sw.siemens.com/documentation/external/PL20200805113346338/en-US/userManual/userguide/html/index.html#page/connect%2Fsplash.html`.
[23] J. Smith, ""journal and rolling element bearings: Advantages/disadvantages of both"," *Vibration Analysis*, 5/4/2022. [Online]. Available: `https://ivctechnologies.com/2022/04/04/journal-and-rolling-element-bearings-advantages-disadvantages-of-both/`.
[24] Tekniska Museet, "Kullager", 2021. [Online]. Available: `https://www.tekniskamuseet.se/lar-dig-mer/100-innovationer/kullager/` (Accessed on: 30/4/2025).
[25] M.-H. Kim and H. Kim, *Hydrostatic, Aerostatic abd Hybrid Bearing Design*. Elsevier, 2012, pp. 1–3.
[26] C. M. Lubricants, *Marine Lubricant Handbook*. Chevron Marine Lubricants, 2023, Information Bulletin 6.
[27] E. M. Corporation, *Safety Data Sheet*. Exxon Mobil Corporation, 2024.

A

Appendix 1

A.1 Matlab Code

```
function [M_120, F_120, F_loc_x, F_loc_y, p_max,p_min]= ExtractData
    (filename)

warning('off')
data = readtable(filename);
warning('on')

cell_index      =  data.CellIndex;
area            =  data.Area_Magnitude_m_2_;     % m^2
wall_shear_x    =  data.WallShearStress_i__Pa_; % Pa
wall_shear_y    =  data.WallShearStress_j__Pa_; % Pa
wall_shear_z    =  data.WallShearStress_k__Pa_; % Pa
pressure        =  data.Pressure_Pa_;           % Pa
x               =  data.X_m_;                   % m
y               =  data.Y_m_;                   % m
z               =  data.Z_m_;                   % m
F_120           =  0;                           % N
M_y             =  0;                           % Nm
M_x             =  0;                           % Nm
p_max           =  0;                           % Pa
ang             = [5.31 14.77 26.66 38.55];     % Degrees
d_theta         = 2;                            % Degrees
r_exclude_inner = 288/2000;                     % m
r_exclude_outer = 320/2000;                     % m

ang             = ang + (1-d_theta)/2;
numCells = length(cell_index);

% Initiate global momentum variable
M_120 = 0;

% Iterate and calculated moment contribution for each element
for element = 1:numCells
    % Extract element values
    ex = x(element);
    ey = y(element);
    r  = [x(element),y(element),z(element)]';
    [etheta, er] = cart2pol(r(1),r(2));
    etheta = etheta *180/pi;
    ep = pressure(element);
    etau = [wall_shear_x(element);wall_shear_y(element);
```

```
    wall_shear_z(element)];
41      eArea = area(element);
42
43      if er > r_exclude_inner &&  er < r_exclude_outer
44          check_var = floor((ang+d_theta-abs(etheta))/d_theta);
45          if ~ismember(0,check_var)
46              if ep > p_max
47                  p_max = ep;
48              end
49          end
50      else
51          if ep > p_max
52              p_max = ep;
53          end
54      end
55
56
57      % Calculate total force at element and the contribution it has
    for a
58      % moment around x and y axis.
59      eF    = ep    *  eArea;
60      eF_v  = etau  *  eArea;
61      eM_v  = cross(r,eF_v);
62      M_y   = M_y   +  eF*ex;
63      M_x   = M_x   +  eF*ey;
64      F_120 = F_120 +  eF;
65
66      % Total moment contribution for element
67      eM_z = eM_v(end);
68
69      % Add element contribution to total moment
70      M_120 = M_120 + eM_z;
71
72  end
73  p_min = min(pressure);
74  F_loc_x = M_y/F_120;
75  F_loc_y = M_x/F_120;
76
77
78  end
```

```
1   function M_r = NmPerRadFunc(filename,r_inner,r_outer,theta_min,
    numSteps,intervalls)
2
3   warning('off')
4   data = readtable(filename);
5   warning('on')
6
7   cell_index      =  data.CellIndex;                  % -
8   area            =  data.Area_Magnitude_m_2_;        % m^2
9   pressure        =  data.Pressure_Pa_;               % Pa
10  x               =  data.X_m_;                       % m
11  y               =  data.Y_m_;                       % m
12  [theta, r]      =  cart2pol(x,y);                   % [Rad, m]
13  M_r             =  zeros(numSteps,1);               % Nm
14  alpha           =  atan(0.02/(r_outer-r_inner));    % -
```

```
numCells        =  length(cell_index);              % -

for element = 1:numCells
    % Extract element values
    ex = x(element);
    ey = y(element);
    ep = pressure(element);
    er = r(element);
    lever = (er-r_inner)/cos(alpha);
    et = theta(element);
    eArea = area(element);

    % Calculate total force at element and the contribution it has for a
    % moment around x and y axis.
    eF      = ep    *  eArea;
    M_inner = eF * lever;

    index = floor((et-theta_min)/intervalls)+1;
    M_r(index) = M_r(index) + M_inner;
end

end
```

```
function [low_p, low_many] = ExtractLowestAbsPressure(filename,n)
warning('off')
data = readtable(filename);
warning('on')

absP        = data.AbsolutePressure_Pa_;

absP_sorted = sort(absP);
low_p = min(absP);
low_many = absP_sorted(1:n);
end
```

```
clear all; close all; clc

%% Variable Initiations

% Initiate variables with base of the filenames
all_filenames = ["Original.csv", "Shallow.csv" "Fillet2.csv" "
    Fillet5.csv","Basic.csv", "OriginalThick.csv","OriginalThin.csv
    ","BasicThick.csv","BasicThin.csv"]; %

loss_filenames  = ["Original.csv" "Shallow.csv" "Fillet2.csv" "
    Fillet5.csv","Basic.csv"]; %

stiffness_filenames = ["OriginalThick.csv","OriginalThin.csv","
    Imbalance Original.csv","BasicThick.csv","BasicThin.csv","
    Imbalance Basic.csv"]; %



% Initiate variables
RPM             =  500;                             % RPM
```

```
omega           =  2*pi/60 * RPM;                    % rad/s
nDiscs          =  7;                                % -
num_steps       =  120;                              % -
r_inner         =  0.1138;                           % m
r_outer         =  0.19;                             % m
theta_min       =  -60*pi/180;                       % Rad
theta_max       =  60*pi/180;                        % Rad
intervalls      =  (theta_max-theta_min)/num_steps;  % Rad
plot_iter_base  =  100;                              % -
max_char        =  length(loss_filenames{1});        % -
min_char        =  length(loss_filenames{1});        % -
num_lowest_abs  =  30;                               % -

% Initiate empty dictionaries and matrices
num_l_files     = length(loss_filenames);
num_s_files     = length(stiffness_filenames);
num_files       = length(all_filenames);
Moment_360      = dictionary(all_filenames,zeros(1,num_files));
Moment_disc     = dictionary(all_filenames,zeros(1,num_files));
Power_360       = dictionary(all_filenames,zeros(1,num_files));
Power_disc      = dictionary(all_filenames,zeros(1,num_files));
Power_tot       = dictionary(all_filenames,zeros(1,num_files));
p_max           = dictionary(all_filenames,zeros(1,num_files));
p_min           = dictionary(all_filenames,zeros(1,num_files));
p_abs_min       = dictionary(all_filenames,zeros(1,num_files));
Force           = dictionary(all_filenames,zeros(1,num_files));
X_loc           = dictionary(all_filenames,zeros(1,num_files));
Y_loc           = dictionary(all_filenames,zeros(1,num_files));
M_r_index       = dictionary(stiffness_filenames,1:num_s_files);
M_r             = zeros(num_steps,num_s_files);
lowest_abs_all  = zeros(num_lowest_abs,num_files);

%% Section For Losses
for filename = all_filenames
    filenameLosses = sprintf('%sLosses.csv',filename{1}(1:end-4));
    len = length(filename{1});

    if len < min_char
        min_char = len;
    elseif len > max_char
        max_char = len;
    end

    [Mom_120,For_120,x_loc,y_loc,p_max_file,p_min_file] =
   ExtractData(filenameLosses);

    % Calculate Torques and Power for disc sides, disc and machine
    Moment_360(filename)    =  3 * Mom_120;
    Power_360(filename)     =  3 * abs(Mom_120) * omega;
    Moment_disc(filename)   =  3 * Mom_120 * 2;
    Power_disc(filename)    =  3 * abs(Mom_120) * omega * 2;
    Power_tot(filename)     =  3 * abs(Mom_120) * omega * 2 *
   nDiscs;
    p_max(filename)         =  p_max_file;
    p_min(filename)         =  p_min_file;
    % Calculate Total Force from pressure and the corresponding x
```

```
    and y
70      % location
71      Force(filename)          =  For_120;
72      X_loc(filename)          =  x_loc;
73      Y_loc(filename)          =  y_loc;
74
75  end
76
77  % Calculate disc properties for displaced discs
78  for i = 1:length(stiffness_filenames)/3
79      files = [3*i-2,3*i-1];
80      Power_disc(stiffness_filenames(files))  = sum(Power_360(
        stiffness_filenames(files)))*ones(1,2);
81      Power_tot(stiffness_filenames(files))   = Power_disc(
        stiffness_filenames(files))*nDiscs;
82      Moment_disc(stiffness_filenames(files)) = sum(Moment_360(
        stiffness_filenames(files)))*ones(1,2);
83  end
84
85  % Print calculted variables
86
87  for filename = all_filenames
88      len = length(filename{1});
89      extension = string(repelem(' ',max_char-length(filename{1})));
90
91      if abs(p_min(filename)/1000)<100
92          extension_p_min = ' ';
93      else
94          extension_p_min = '';
95      end
96
97      printing_string = sprintf("| Sim: %s %s | p_max: %.1f [kPa] |
        p_min: %.1f %s [kPa] | T_120 = %.4f [Nm] | T_disc: %.4f [Nm] |
        P_disc: %.1f [W] | P_tot: %.2f [W] |  F_p: %.2f [N] | F_p Coord:
         X = %.1f [mm], Y = %.1f [mm] |\n",...
98          string(filename{1}(1:end-4)),extension,p_max(filename)
        /1000,p_min(filename)/1000,extension_p_min, Moment_360(filename)
        /3,Moment_disc(filename) ,Power_disc(filename),Power_tot(
        filename), Force(filename), X_loc(filename)*1000, Y_loc(filename
        )*1000);
99      dashed_line = repelem('-',length(printing_string{1}));
100     fprintf(string(dashed_line) + "\n")
101     fprintf(printing_string)
102     if strcmp(filename,all_filenames(end))
103         fprintf(string(dashed_line) + "\n")
104     end
105 end
106
107 %% Section For Rigidness
108 for filename = stiffness_filenames([1,2,4,5])
109     filenameLosses                = sprintf('%sLosses.csv',filename
        {1}(1:end-4));
110     M_r_file                      = NmPerRadFunc(filenameLosses,
        r_inner,r_outer,theta_min,num_steps,intervalls);
111     M_r(:,M_r_index(filename))    = M_r_file;
112 end
```

```
113
114 % Get imbalance torques
115 M_r(:,3) = M_r(:,M_r_index("OriginalThin.csv"))-M_r(:,M_r_index("
    OriginalThick.csv"));
116 M_r(:,6) = M_r(:,M_r_index("BasicThin.csv"))-M_r(:,M_r_index("
    BasicThick.csv"));
117
118 theta = 1:num_steps;
119 theta = (2.*theta+1).*intervalls;
120
121 for j = 1:num_s_files
122
123     % Print each Angular Sections Torque
124     figure()
125     % Retreive torque from one element and add to sections total
    torque
126     for i = 1:num_steps
127         [ex,ey] = pol2cart([i-1, i-1, i, i]*intervalls+theta_min+pi
    /2, [r_inner r_outer r_outer r_inner]);
128         if j == M_r_index("OriginalThick.csv") || j==M_r_index("
    BasicThick.csv")
129             a = -1;
130         else
131             a = 1;
132         end
133         fill(ex,ey,a*M_r(i,j), EdgeColor='none')
134         hold on
135     end
136
137     % Plot colorshaded torque plot
138     [x_inner,y_inner] = pol2cart(linspace(theta_min,theta_max,
    num_steps)+pi/2,ones(1,num_steps)*r_inner);
139     plot(x_inner,y_inner,'--k',LineWidth=1.5);
140     set(gca,'DataAspectRatio',[1 1 1])
141     c = colorbar('southoutside');
142     c.Label.String = '[Nm]';
143     colormap jet
144     xlabel('X [m]');
145     ylabel('Y [m]');
146     title_string = sprintf('Torque Response %s',stiffness_filenames
    {j}(1:end-4));
147     title(title_string)
148
149     % Print torque as a function of the Angle
150     figure()
151     plot(flip(theta),M_r(:,j)/intervalls,'r',linewidth=1.5)
152     hold on
153     xlabel('Theta [rad]');
154     ylabel('Torque [Nm/rad]');
155     title_string = sprintf('Torque Function of Angle %s',
    stiffness_filenames{j}(1:end-4));
156     title(title_string)
157     grid on
158
159 end
160 %% Residual Plotting
```

```
161
162 for filename = all_filenames
163
164     % Create string to get correct filenames
165     residual_name = sprintf('%sRes%s',filename{1}(1:end-4),filename
    {1}(end-3:end));
166     conv_name = sprintf('%sConverganceVars%s',filename{1}(1:end-4),
    filename{1}(end-3:end));
167
168     % Retreive data from .csv files
169     warning('off')
170     residual_data = readtable(residual_name);
171     conv_data = readtable(conv_name);
172     warning('on')
173
174     % Put residual data to variables
175     iter_res     = residual_data.Iteration;
176     Conitnuity   = residual_data.Continuity_Residual;
177     x_mom        = residual_data.X_momentum_Residual;
178     y_mom        = residual_data.Y_momentum_Residual;
179     z_mom        = residual_data.Z_momentum_Residual;
180     sdr          = residual_data.Sdr_Residual;
181     tke          = residual_data.Tke_Residual;
182     figure;
183
184     % Plot residuals
185
186     semilogy(iter_res,Conitnuity,'b',Linewidth=1.25);
187     hold on
188     semilogy(iter_res,x_mom ,'r',Linewidth=1.25);
189     semilogy(iter_res,y_mom ,'y',Linewidth=1.25);
190     semilogy(iter_res,z_mom ,Linewidth=1.25);
191     semilogy(iter_res,sdr ,'k',Linewidth=1.25);
192     semilogy(iter_res,tke,'g',linewidth=1.25)
193     legend('Continuity','X Momentum','Y Momentum','Z Momentum','Sdr
    ','Tke', Location='northeast')
194     grid on
195     xlabel('Iteration [-]');
196     ylabel('Residual [-]');
197     title(sprintf('Residuals for %s',filename{1}(1:end-4)))
198
199
200     % Fix issue with some simulation calculating key variables
    every
201     % iteration instead of every tenth
202     if ismember(1,isnan(conv_data{:,:}))
203         [row,column] = find(isnan(conv_data{:,:}) == 1);
204
205         if max(row)> plot_iter_base
206             start_iter_plot = max(row);
207         else
208             start_iter_plot = plot_iter_base;
209         end
210
211     else
212         start_iter_plot = plot_iter_base;
```

```
    end

    % Initiate variables for key variables
    star_iter_index = find(conv_data{:,1} == start_iter_plot);
    iter_mass       = conv_data{:,1}(star_iter_index:end);
    x_c             = conv_data{:,2}(star_iter_index:end).*1000;
    y_c             = conv_data{:,3}(star_iter_index:end).*1000;
    F               = conv_data{:,4}(star_iter_index:end);
    IF1             = conv_data{:,5}(star_iter_index:end);
    IF2             = conv_data{:,6}(star_iter_index:end);
    inlet_flw       = conv_data{:,7}(star_iter_index:end);
    outlet_i_flw    = conv_data{:,8}(star_iter_index:end);
    outlet_o_flw    = conv_data{:,9}(star_iter_index:end);
    torque          = conv_data{:,10}(star_iter_index:end);

    % Plot all key variables
    figure;
    plot(iter_mass,x_c,'r',Linewidth=1.25);
    hold on
    plot(iter_mass,y_c,'b',Linewidth=1.25);
    grid on
    legend('Center of Loads X', 'Center of Loads Y',Location='east'
)
    ylabel('Millimeter');
    xlabel('Iteration [-]');
    title(sprintf('Center of load coordinates on rotor for %s',
filename{1}(1:end-4)))
    xlim([start_iter_plot, iter_mass(end)])
    figure;
    plot(iter_mass,F,'r',Linewidth=1.25)
    grid on
    ylabel('Force [N]')
    xlabel('Iteration [-]');
    title(sprintf('Force on rotor in Z-direction for %s',filename
{1}(1:end-4)))
    xlim([start_iter_plot-10, iter_mass(end)+10])

    figure;
    plot(iter_mass,torque,'r',Linewidth=1.25)
    grid on
    ylabel('Torque [Nm]')
    xlabel('Iteration [-]');
    title(sprintf('Torque on rotor for %s',filename{1}(1:end-4)))
    xlim([start_iter_plot-10, iter_mass(end)+10])

    figure;
    plot(iter_mass ,inlet_flw,'b',Linewidth=1.25);
    hold on
    plot(iter_mass ,outlet_i_flw ,'r',Linewidth=1.25);
    plot(iter_mass,outlet_o_flw ,'c',Linewidth=1.25);
    plot(iter_mass,IF1 ,'g',Linewidth=1.25);
    plot(iter_mass,IF2 ,'m',Linewidth=1.25);
    plot(iter_mass,outlet_i_flw+outlet_o_flw+inlet_flw+IF1+IF2,'k',
linewidth=1.25)
    legend('Inlet','Outlet Inner','Outlet Outer','IF1','IF2','Sum
of Flow', location='southeast')
```

```
264     grid on
265     xlabel('Iteration [-]');
266     ylabel('Mass Flow [g/s]');
267     title(sprintf('Mass Flows for %s',filename{1}(1:end-4)))
268     xlim([start_iter_plot, iter_mass(end)])
269     ylim([-100,100])
270 
271 end
272 
273 %% Section for Lowest ABS Pressure
274 k=1;
275 for filename = all_filenames
276     filneamePressure = sprintf('%sPressure.csv',filename{1}(1:end
    -4));
277     [p_abs_min_file , p_abs_min_many_file] =
    ExtractLowestAbsPressure(filneamePressure,num_lowest_abs);
278     lowest_abs_all(:,k) = p_abs_min_many_file;
279     k=k+1;
280     p_abs_min(filename) = p_abs_min_file;
281 end
282 
283 all_filenames
284 lowest_abs_all
```

A.2 Residuals for Remaining Geometries

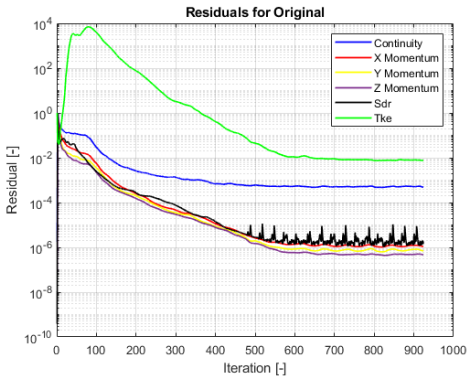

Figure A.1: Residuals for Original Geometry

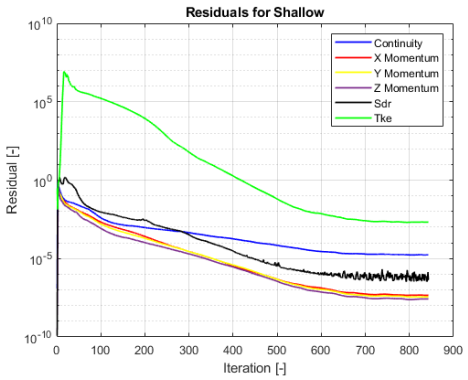

Figure A.2: Residuals for Shallow Pocket Geometry

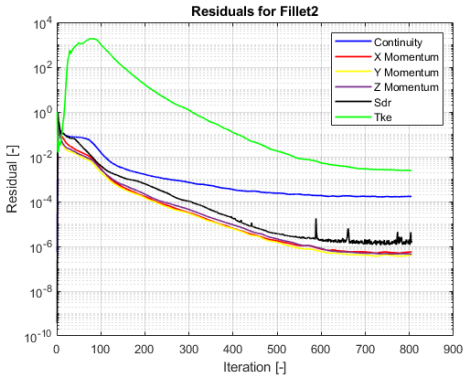

Figure A.3: Residuals for 2 mm Fillet Geometry

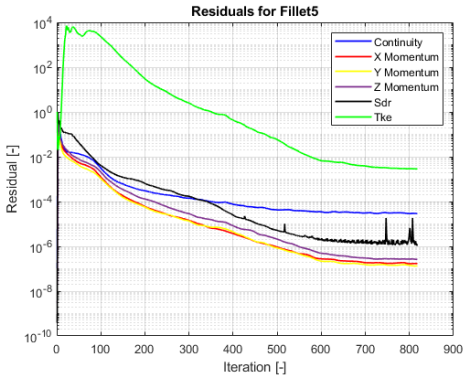

Figure A.4: Residuals for 5 mm Fillet Geometry

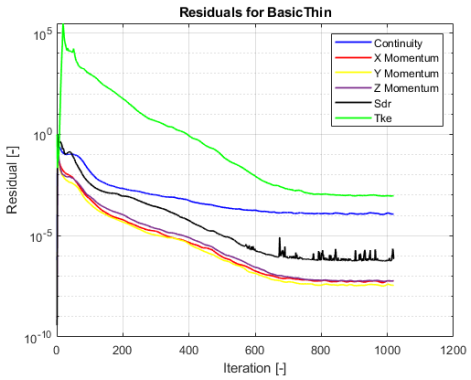

Figure A.5: Residuals for Basic Thinner Gap Geometry

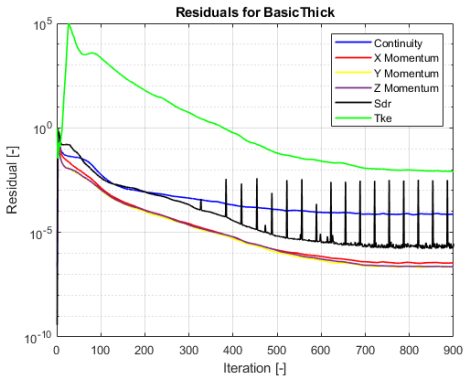

Figure A.6: Residuals for Basic Thicker Gap Geometry

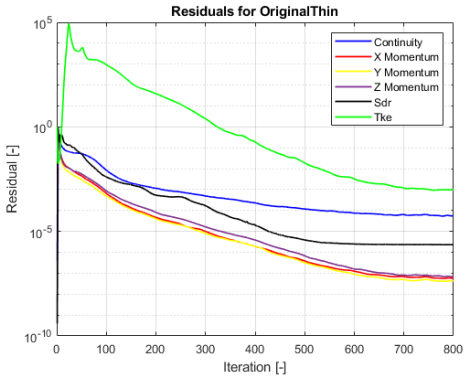

Figure A.7: Residuals for Original Thinner Gap Geometry

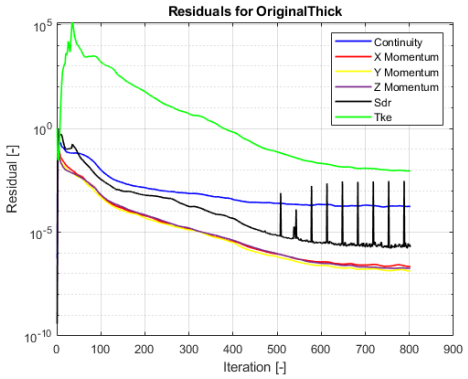

Figure A.8: Residuals for Original Thicker Gap Geometry

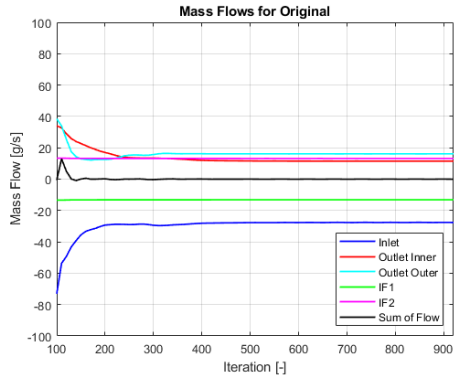

Figure A.9: Mass Flows for Original Geometry

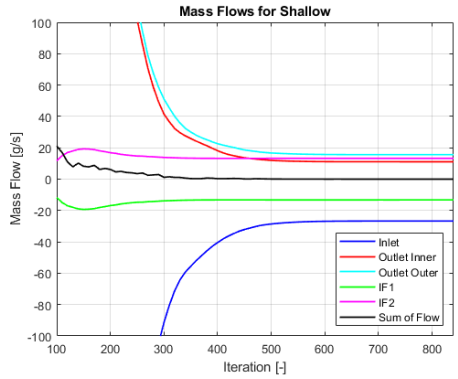

Figure A.10: Mass Flows for Shallow Pocket Geometry

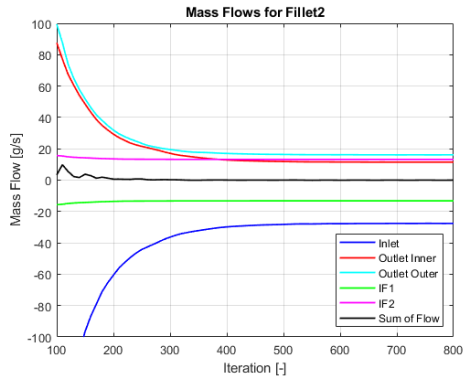

Figure A.11: Mass Flows for 2 mm Fillet Geometry

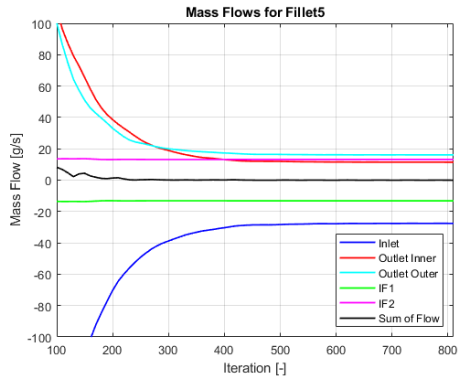

Figure A.12: Mass Flows for 5 mm Fillet Geometry

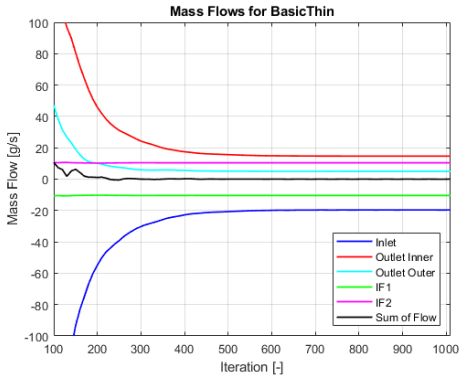

Figure A.13: Mass Flows for Basic Thinner Gap Geometry

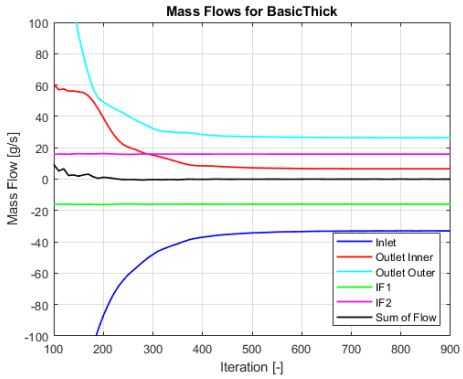

Figure A.14: Mass Flows for Basic Thicker Gap Geometry

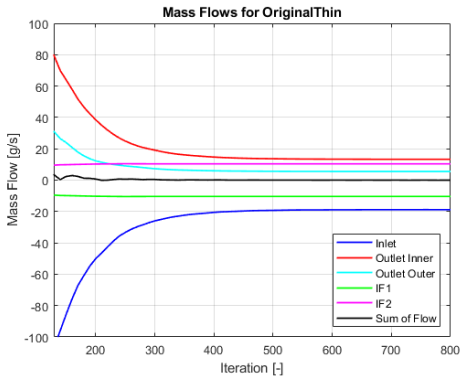

Figure A.15: Mass Flows for Original Thinner Gap Geometry

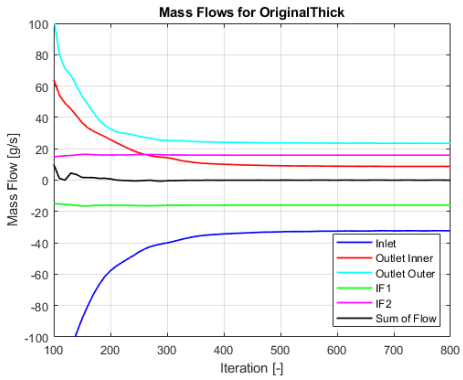

Figure A.16: Mass Flows for Original Thicker Gap Geometry

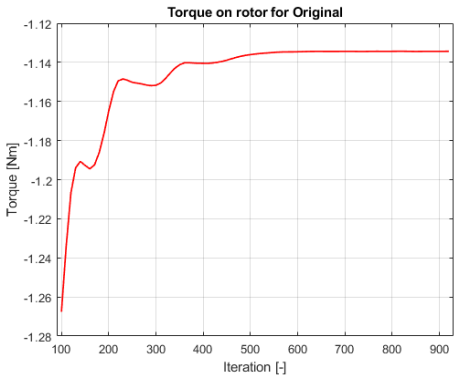

Figure A.17: Torque Around Z-Axis on Rotor Surface for Original Geometry

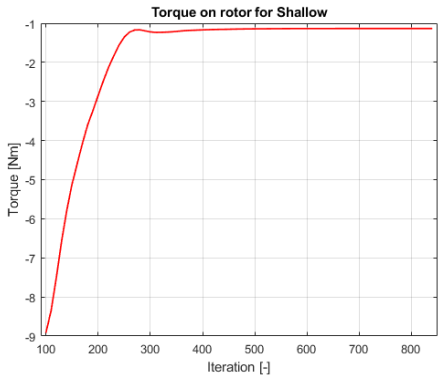

Figure A.18: Torque Around Z-Axis on Rotor Surface for Shallow Pocket Geometry

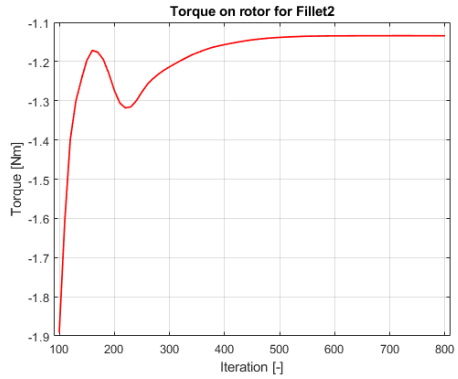

Figure A.19: Torque Around Z-Axis on Rotor Surface for 2 mm Fillet Geometry

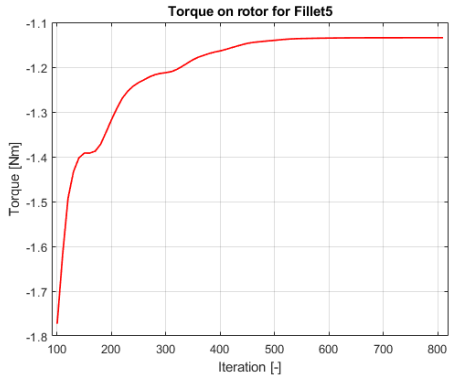

Figure A.20: Torque Around Z-Axis on Rotor Surface for 5 mm Fillet Geometry

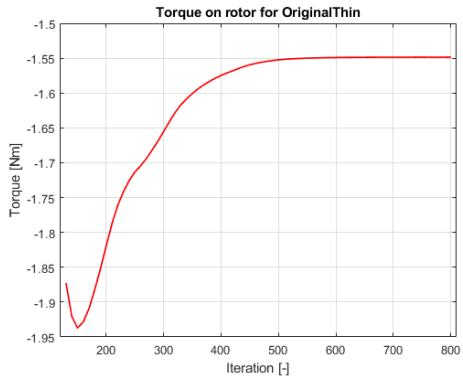

Figure A.21: Torque Around Z-Axis on Rotor Surface for Original Thinner Gap Geometry

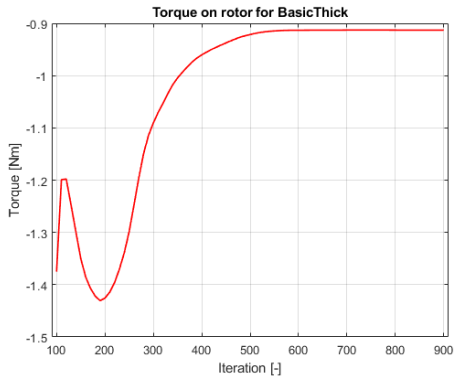

Figure A.22: Torque Around Z-Axis on Rotor Surface for Basic Thicker Gap Geometry

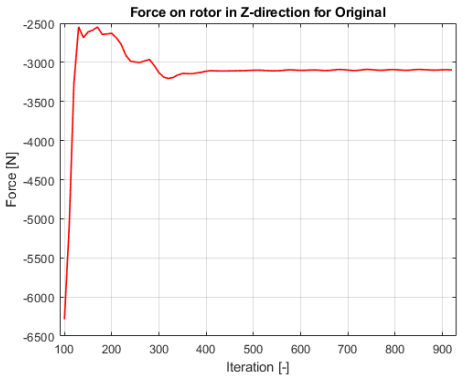

Figure A.23: Force in Z-Direction on Rotor Surface for Original Geometry

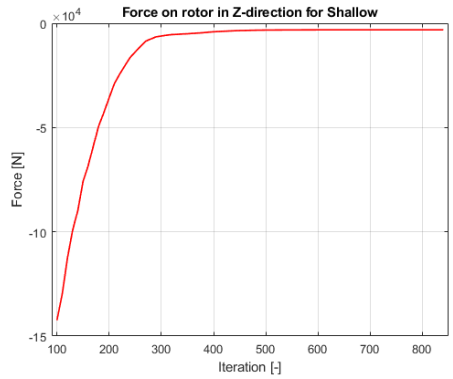

Figure A.24: Force in Z-Direction on Rotor Surface for Shallow Pocket Geometry

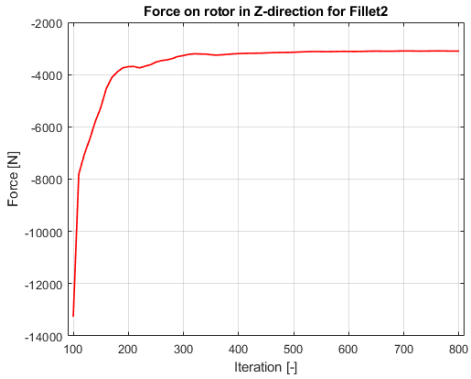

Figure A.25: Force in Z-Direction on Rotor Surface for 2 mm Fillet Geometry

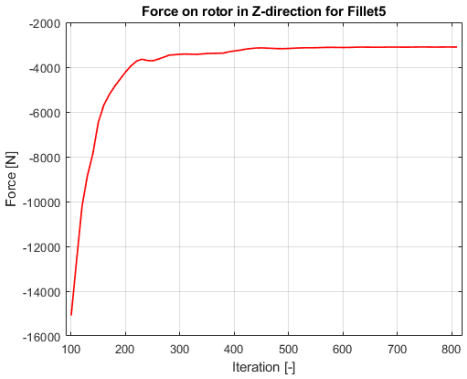

Figure A.26: Force in Z-Direction on Rotor Surface for 5 mm Fillet Geometry

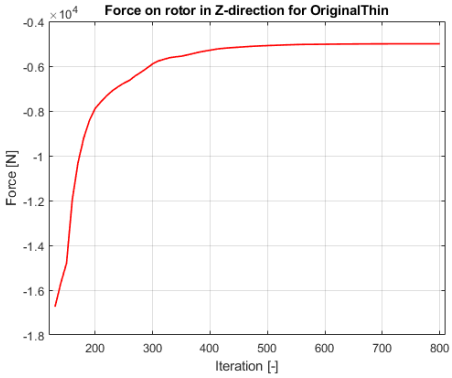

Figure A.27: Force in Z-Direction on Rotor Surface for Original Thinner Gap Geometry

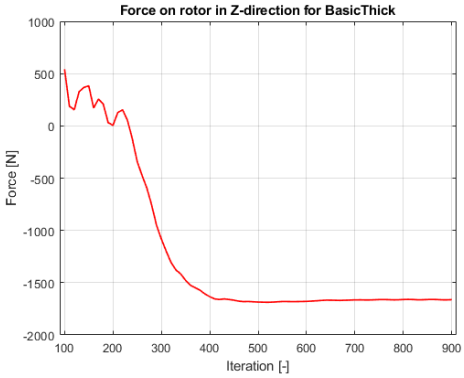

Figure A.28: Force in Z-Direction on Rotor Surface for Basic Thicker Gap Geometry

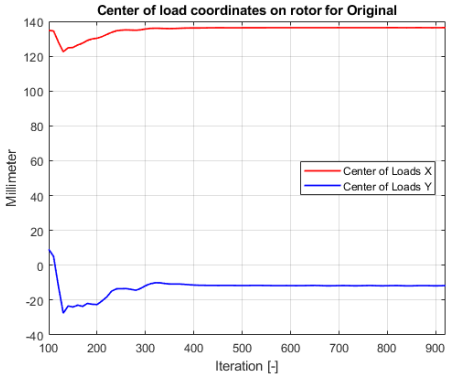

Figure A.29: Centre of Load Coordinates for Original Geometry

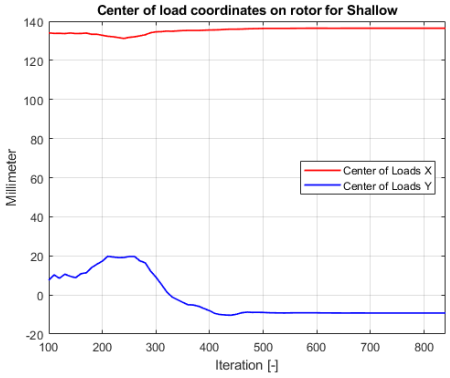

Figure A.30: Centre of Load Coordinates for Shallow Pocket Geometry

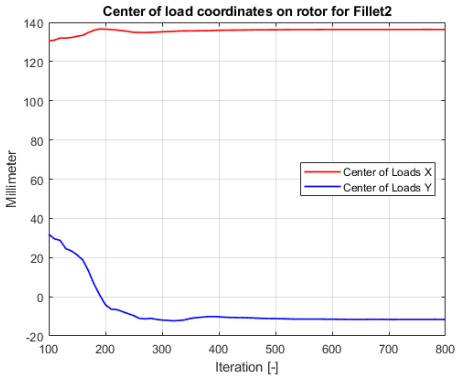

Figure A.31: Centre of Load Coordinates for 2 mm Fillet Geometry

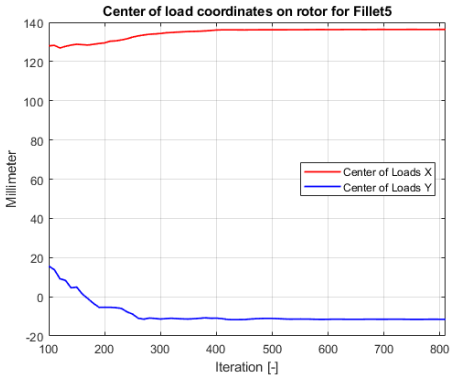

Figure A.32: Centre of Load Coordinates for 5 mm Fillet Geometry

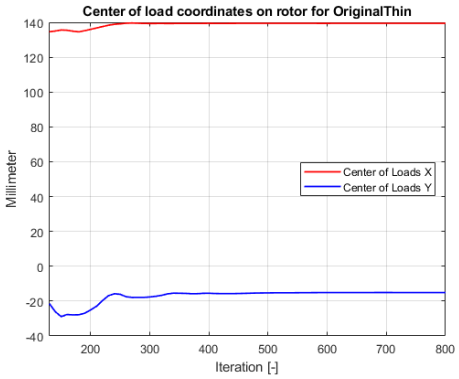

Figure A.33: Centre of Load Coordinates for Original Thinner Gap Geometry

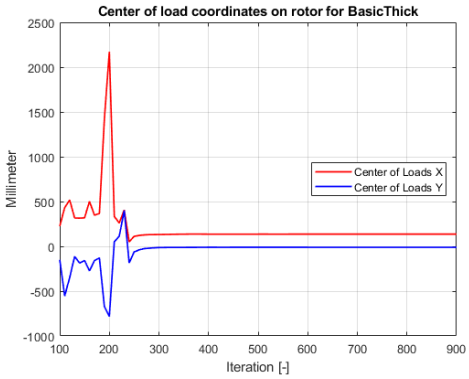

Figure A.34: Centre of Load Coordinates for Basic Thicker Gap Geometry

DEPARTMENT OF MECHANICS AND MARITIME SCIENCE
CHALMERS UNIVERSITY OF TECHNOLOGY
Gothenburg, Sweden
www.chalmers.se

CHALMERS
UNIVERSITY OF TECHNOLOGY